Enhancing corrosion resistance of XC38 steel using sulfur and nitrogen-containing phenyl thiosemicarbazone: A comprehensive experimental and computational analysis

Smail Brioua [a], Amel Delimi [b,c], Hana Ferkous [b,c,*], Said Boukerche [d,e], Hamza Allal [c], Abir Boublia [f], Amel Djedouani [g,h], Malika Berredjem [i], Abdesalem Kahlouche [j], Khadidja Otmane Rachedi [i], Amdjed Abdennouri [k], Manawwer Alam [l], Barbara Ernst [m], Yacine Benguerba [n,*]

[a] Département de Chimie, Faculté des Sciences, Université de 20 août 1955 de Skikda, Skikda, 21000, Algeria
[b] Laboratory of Mechanical Engineering and Materials, Faculty of Technology, University 20 August 1955 - Skikda, 21000, Skikda, Algeria
[c] Département de Technologie, Université de 20 août 1955 de Skikda, Skikda, 21000, Algeria
[d] Department of Material Sciences, Faculty of Science and Technology, University Mohamed Cherif Messaadia of Souk Ahras, 41000, Algeria
[e] Laboratory of Surface Engineering (LIS), University Badj iMokhtar of Annaba, 23000, Algeria
[f] Laboratoire de Physico-Chimie des Hauts Polymères (LPCHP), Département de Génie des Procédés, Faculté de Technologie, Université Ferhat ABBAS Sétif-1, Sétif, 19000, Algeria
[g] Laboratoire de Physicochimie Analytique et Cristallochimie des Matériaux Organométalliques et Biomoléculaires, Université Constantine 1, 25000, Constantine, Algeria
[h] Ecole Normale Supérieure de Constantine, Ville Universitaire Ali Mendjeli, 25000, Constantine, Algeria
[i] Laboratory of Applied Organic Chemistry LCOA. Synthesis of Biomolecules and Molecular Modelling Group, University Badji-Mokhtar, Annaba. Box 12. 23000, Annaba, Algeria
[j] CRTI Research Centre in Industrial Technologies, CRTI P.O.Box 64, Cheraga 16014, Algiers, Algeria
[k] Laboratoire de Physico-Chimie des Surfaces et des Interfaces, Université 20 août 1955 de Skikda, BP 26, Route El Hadaik, 21000, Skikda, Algeria
[l] Department of Chemistry, College of Science, King Saud University, PO Box 2455, Riyadh, 11451, Saudi Arabia
[m] Université de Strasbourg, CNRS, IPHC UMR 7178, Laboratoire de Reconnaissance et Procédés de Séparation Moléculaire (RePSeM), ECPM 25 rue Becquerel, F-67000, Strasbourg, France
[n] Laboratoire de Biopharmacie Et Pharmacotechnie (LBPT), Université Ferhat ABBAS Sétif-1, Sétif, Algeria

ARTICLE INFO	ABSTRACT
	Background: This research explores the effectiveness of a novel Schiff base compound as an organic corrosion inhibitor for XC38 steel immersed in a 1M hydrochloric acid solution. The study aims to identify the inhibitor's ability to reduce corrosion under controlled experimental conditions. *Methods:* The synthesis and characterization of the Schiff base inhibitor were meticulously confirmed through FTIR, XRD, and NMR techniques. The efficacy of this inhibitor in curbing the corrosion of XC38 carbon steel in a 1M hydrochloric acid solution was rigorously evaluated using gravimetric analysis, Electrochemical Impedance Spectroscopy (EIS), and Potentiodynamic Polarization (PDP), with a specific focus on the impacts of varying concentrations and temperatures. Surface interaction mechanisms were thoroughly investigated using SEM, EDS, AFM, ATR-FTIR, and XRD. These studies were complemented by activation thermodynamics and adsorption isotherm assessments, providing a comprehensive understanding of the thermodynamic properties of the inhibitor. Additionally, computational studies, including DFT, NCI analysis, and MC simulations, were employed to delve into the dynamics of inhibitor-surface interactions, offering detailed insights into the molecular interactions at play. *Significant findings:* The novel Schiff base inhibitor demonstrated remarkable efficacy, achieving up to 98.14 % effectiveness at a concentration of 100 ppm in protecting XC38 steel in a corrosive environment as determined by weight loss measurements. Gravimetric analysis revealed a significant reduction in mass loss and corrosion rate, corresponding with an increase in DMTS concentration. PDP measurements indicated an inhibition efficiency (EI %) of up to 94 %. EIS results showed an inhibition efficiency (EI%) of up to 93.53 %. The inhibitor's performance

was notably enhanced at lower temperatures (303, 313, and 323 K) and higher concentrations. Activation thermodynamics and adsorption isotherm studies showed negative ΔG_{ads}° values, indicating spontaneous adsorption. Advanced EIS and Tafel polarization studies identified the compound as a mixed-type inhibitor, effectively modulating both cathodic and anodic reactions. Surface analyses using SEM, EDS, AFM, and XRD confirmed the formation of a protective layer on the steel surface, preventing the formation of iron oxides and thus mitigating corrosion. Complementary DFT calculations, including analyses of Mulliken charge, FMOs, DOS, ESP, and ELF analyses, provided detailed insights into potential electron donation and acceptance sites crucial for its inhibitory action. NCI analysis shed further light on the nature of inhibitor-metal surface interactions, enhancing our understanding of the adsorption mechanisms. MC simulations robustly supported these theoretical insights, which depicted the inhibitor's adsorption behavior on the Fe(110) surface, demonstrating a compelling alignment between theoretical forecasts and empirical observation.

1. Introduction

Pure metals and alloys undergo chemical or electrochemical reactions in corrosive conditions, which generate a stable combination and ultimately lead to metal loss [1–5]. Despite being extensively employed in diverse industries such as transportation, construction, and defense because of its superior mechanical and physical qualities, low cost, and high strength [6–9], carbon steel is renowned for its susceptibility to corrosion. Per the ISO 8044 standard [6], corrosion transpires when electrochemical physicochemical exchanges transpire between an environment and a metallic material, resulting in alterations to the material's composition. Such modifications can potentially detrimentally impact the substance's functionality, the surrounding environment, or any technical system it contributes to [7–9].

As a result of the considerable financial implications associated with corrosion, several strategies have been developed to mitigate, prevent, or even eliminate its impact [10,11]. Among these methods, corrosion inhibitors are particularly noteworthy as a crucial instrument for controlling and averting corrosion [12,13]. Significantly influencing its efficacy is the level of contact that an inhibitor of corrosion has with the metal's surface. As an example, adsorption inhibitors have the potential to influence the corrosion process via two mechanisms: generating a layer of protection on the surface of the metal or changing the activation barriers of corrosion-related anodic and cathodic processes [14,15].

The scientific literature has shown several Schiff bases' exceptional corrosion inhibitory properties for metals and alloys subjected to acidic environments [16–18]. Schiff bases are often used in corrosion inhibition due to their facile synthesis and non-toxic or low toxicity [19]. This is due to the detrimental environmental effects of corrosion inhibitors and the long-term financial and operational advantages of corrosion-resistant carbon steel [20,21].

Organic inhibitors' inhibitory effect is enhanced by incorporating heteroatoms (nitrogen, sulfur, oxygen, and phosphorus) and the imine functional group into their structures [22–24]. Adsorption coatings fabricated using these compounds are often exceedingly thin and durable; they provide corrosion protection by impeding cathodic or anodic reactions or both [25,26]. The efficacy of inhibitors is contingent upon the surrounding medium, the adsorption surface structure of the metal, as well as the electrochemical potential at the point of contact [27,28]. Simultaneously, the protected region on the metal surface, molecule size, adsorption mechanism, and charge density influence their effectiveness [29–32].

This study evaluates the corrosion inhibitory properties of 3,4-dimethoxy phenyl thiosemicarbazone (DMTS) on XC38 carbon steel within a 1 M hydrochloric acid (HCl) environment. The selection of DMTS as a corrosion inhibitor is based on its molecular structure, which includes multiple heteroatoms (nitrogen, sulfur, and oxygen) and an imine group, known to enhance corrosion inhibition. These functional groups facilitate the formation of a stable and protective adsorption layer on the metal surface, thereby impeding corrosion processes. The choice of XC38 carbon steel is particularly relevant due to its widespread industrial applications, including in construction, automotive, and manufacturing sectors. XC38 steel is known for its moderate carbon content, which provides a balance of strength, ductility, and hardness [13,33–36]. However, its susceptibility to corrosion in acidic environments, such as those encountered in oil well acidification, steel pickling, chemical cleaning, and various industrial processes, makes it an ideal candidate for evaluating the efficacy of corrosion inhibitors like DMTS. Understanding the corrosion behavior of XC38 steel and developing effective inhibitors is crucial for prolonging the service life of steel components in these harsh environments.

The chemical synthesis of DMTS was rigorously verified using FTIR, XRD, and NMR techniques. The use of a 1 M HCl solution is particularly relevant to real-world industrial conditions, where such acidic environments are frequently employed in processes like oil well acidification, steel pickling, chemical cleaning, and industrial processing. These conditions are known to accelerate corrosion, thus allowing for the rapid observation of corrosion effects within a practical timeframe [37,38]. To thoroughly investigate DMTS's impact on the corrosion of XC38 steel, this research utilizes a diverse set of experimental and computational methods. Techniques such as gravimetric analysis, Potentiodynamic polarization (PDP), electrochemical impedance (EIS) spectroscopy, scanning electron microscopy (SEM), energy-dispersive X-ray spectroscopy (EDS), atomic force microscopy (AFM), Fourier-transform infrared spectroscopy with an attenuated total reflectance accessory (FTIR/ATR). Spectroscopy and X-ray diffraction (XRD) will be employed. Furthermore, density functional theory (DFT) simulations, non-covalent interaction (NCI) studies, and Monte Carlo (MC) simulations will aid in understanding the molecular interactions between DMTS and the metal surface.

This research aims to elucidate the protective effects of DMTS against corrosion of XC38 carbon steel in a 1 M HCl solution, offering vital insights for developing corrosion-resistant materials and coatings for industrial use. It highlights the critical need to understand metal corrosion in acidic environments and develop effective corrosion prevention strategies. The study also introduces a fresh perspective on the anticorrosion capabilities of Schiff base compounds like DMTS, focusing on their action mechanisms and establishing their potential as effective corrosion inhibitors. Moreover, it encourages further exploration into Schiff base compounds and similar materials to enhance understanding of their inhibitory mechanisms. By combining theoretical and experimental approaches, this investigation aims to foster a more comprehensive understanding of corrosion inhibition, which could lead to the creation of safe, efficient, and environmentally friendly corrosion preventive solutions.

2. Experimental methods

2.1. DMTS synthesis

3,4-dimethoxy phenyl thiosemicarbazone (DMTS) is prepared through a specific synthesis process. Initially, an equimolar mixture of 3,4-dimethoxy benzaldehyde and thiosemicarbazide, each at 9 mmol, is combined in 30 ml of absolute ethanol. This mixture acts as the solvent for the reaction. To catalyze the reaction, two drops of glacial acetic acid are added. The presence of glacial acetic acid in this synthesis is crucial

as it facilitates the formation of DMTS by promoting the necessary chemical reactions between benzaldehyde and thiosemicarbazide. This process results in the formation of DMTS, as depicted in Scheme 1 of the study. The method is designed to ensure optimal reaction conditions for producing DMTS with high purity and efficacy, which is essential for its intended use as a corrosion inhibitor.

The synthesis of DMTS involves a series of meticulous steps to ensure the formation of a high-quality product. After preparing the initial mixture, as previously described, the next phase is the reflux process. This involves heating the mixture under reflux for three hours while stirring continuously. Refluxing ensures that the reaction proceeds completely under controlled temperature conditions, allowing the reactants to fully interact and form the desired compound.

Upon completion of the reflux period, the mixture is permitted to cool down to ambient temperature. The cooling process leads to forming of a yellow precipitate, indicative of the formation of DMTS. The precipitate is then separated from the mixture through filtration and washed with ethanol. This step is crucial for removing impurities and unreacted materials, thereby purifying the product.

The final step in the synthesis involves recrystallization, a technique employed to purify the compound further. The yellow precipitate is recrystallized using a solvent mixture comprising 75 % ethanol and 25 % water. This process enhances the purity and crystalline quality of the DMTS, resulting in a final product with a satisfactory yield of 68 %.

Moreover, the interaction of DMTS with metal surfaces in a corrosive environment, particularly in hydrochloric acid, is a key aspect of its functionality as a corrosion inhibitor. As stated in Scheme 2, the efficiency of DMTS in inhibiting corrosion is significantly influenced by the anion concentration on the metal's surface. The cationic form of DMTS, generated in the presence of hydrochloric acid, is adept at adsorbing onto the metal surface. This adsorption is primarily facilitated by the lone pairs of electrons on nitrogen heteroatoms and oxygen in DMTS, which form strong bonds with the empty d orbitals of the metal surface. Additionally, DMTS adheres to the metal surface through electrostatic donor-acceptor interactions arising from electron interactions in the p orbitals of its aromatic systems. These mechanisms underline the compound's effectiveness in providing a protective barrier against corrosion.

In Scheme 2, the protonation of DMTS in an HCl bath is depicted. It is crucial to identify the most acidic nitrogen atom in the molecule for accurate protonation. DMTS contains three nitrogen atoms, each with varying pK_a values. Using Marvin Sketch, we have determined that the nitrogen atom of the thiosemicarbazone group has the highest acidic character, justifying its selection for protonation. The protonation of this nitrogen atom leads to the formation of a cationic species, which enhances the adsorption capability of DMTS on metal surfaces by increasing its electrostatic interactions with the negatively charged sites on the metal.

The nitrogen atom of the imine group acquires an excessively negative charge due to the mesomeric impact of the methoxy group (Scheme 3). Additionally, the donor action of the neighboring nitrogen enhances the sulfur's activation. This electron-donating effect stabilizes

the adsorption of DMTS on the metal surface, further contributing to its corrosion inhibition properties.

2.2. Specimen preparation

XC38 samples of carbon steel were applied in the investigations. The relative abundances of the most basic chemical elements are shown in Table 1. Before initiating the investigation, a sequence of mechanical abrasions with increasingly more abrasive paper was conducted, reaching a grit of 2000. After washing it with distilled water and removing grease with acetone, air dry it. Utilizing 37 % hydrochloric acid, a 1 M HCl solution with corrosive characteristics was created. Concentrations of the inhibitor ranged from 10 to 100 ppm (10, 40, 80, and 100 ppm).

2.3. Corrosion examination

### 2.3.1. Gravimetric investigation

The cylindrical steel samples were immersed vertically inside a 100 ml test tube containing 10 ml electrolyte for the gravimetric measurements. A molar hydrochloric acid solution takes gravimetric measurements on polished and cleaned items, including varying inhibitor doses. To determine the corrosion rate (mg cm^{-2} h^{-1}), specimens are weighed before and after immersion (1, 2, 24 h), accompanied by rinsing with deionized water, drying, acetone cleaning, and further weighing. By submerging metal at room temperature in an acidic solution (1M HCl), one may examine the impact of various extract concentrations on corrosion rates, denoted as Wcorr and W'corr (mg cm^{-2} h^{-1}). Subsequently, the inhibitory efficiency associated with weight loss (E_{wl}) and degree of surface coverage (θ) were calculated utilizing the following equations [39,40]:

$$E_{WL} = \frac{W_{corr} - W'_{corr}}{W_{corr}} \times 100 \qquad (1)$$

$$\theta = \frac{E_{WL}}{100} \qquad (2)$$

2.3.2. Electrochemical analyses

Using EC-LAB V 10.33 and a typical three-electrode cell, we conducted the EIS and PDP. The reference electrode in this configuration is saturated calomel (SCE), whereas the working electrode is carbon steel, and the counter electrode is platinum. The open circuit voltage was swept from −200 mV to +200 mV at a rate of 0.5 mV/s to produce polarization curves. It is eliminated if the electrode remains at the abandonment potential for 45 min. It is feasible to ascertain the magnitude of the voltage difference that separates the working and counter electrodes. Inhibition efficiency (E_{PDP} (%)) was calculated from Icorr using the following equation:
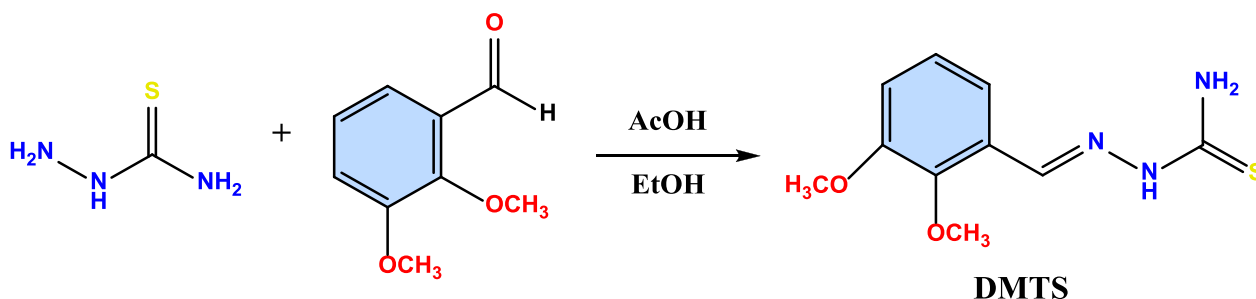
Scheme 1. Synthesis of DMTS.
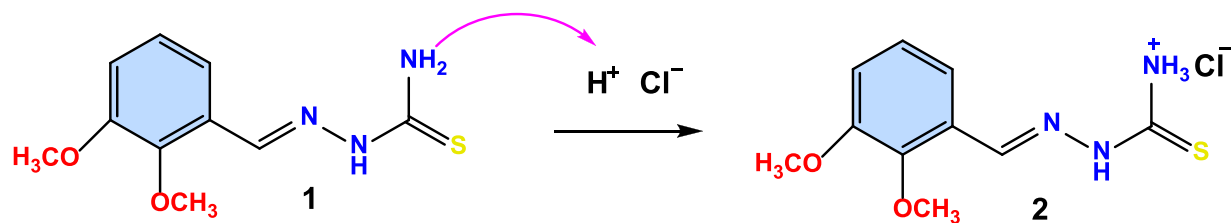
Scheme 2. Protonation of DMTS in HCl bath.
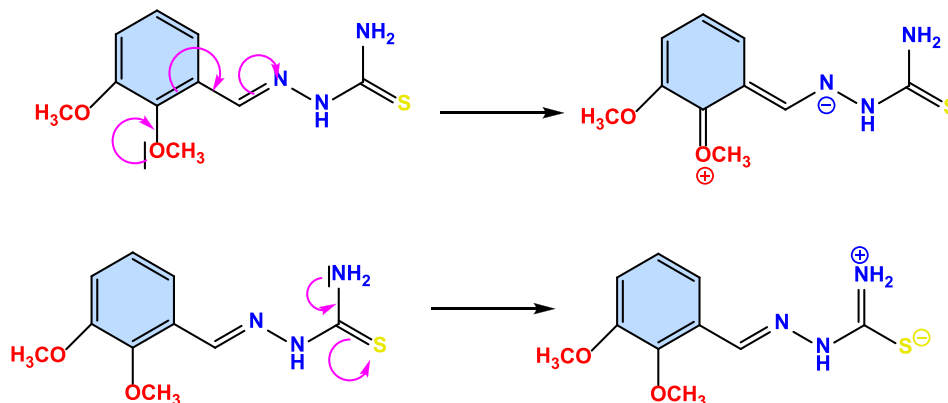
Scheme 3. The capacity of the methoxy and amine groups to donate electrons.

Table 1
XC38 carbon steel chemical composition.

Element	C	Mn	Si	S	P	Fe
Percentage (wt. %)	0.30-0.35	0.05-1.0	0.15-0.35	0.035	0.035	Balance

$$E_{PDP}(\%) = \frac{\left(i_{corr}^{0} - i_{corr}\right)}{i_{corr}^{0}} \times 100 \qquad (3)$$

When inhibitors are present, the corrosion current is i_{corr}, and in the absence of inhibitors is i_{corr}^{0}.

The customary signal used in EIS investigations has an open-circuit voltage amplitude of 10 mV and a peak-to-peak frequency ranging from 100 kHz to 10 MHz. The percentage of inhibitory efficiency E_{EIS} (%) may be calculated using the equation provided by [41]:

$$E_{EIS}(\%) = \frac{\left(R_{ct} - R_{ct}^{0}\right)}{R_{ct}} \times 100 \qquad (4)$$

2.3.3. Surface characterization

We employed advanced microscopy and spectroscopy techniques to evaluate metal samples' surface morphology and elemental composition. Optical microscopy was used for initial observation, providing a broader view of the sample surface. For more detailed analysis, SEM with a TESCAN VEGA-3, operating at 20.0 kV, allowed for high-resolution imaging of the surface structure. For elemental analysis, EDS was integrated with SEM. This powerful technique is designed to detect and quantify the elements present on the surface, which is especially valuable when investigating corrosion and related chemical changes. In this study, we immersed XC38 metal samples in 1 M hydrochloric acid for 72 h, with and without the DMTS corrosion inhibitor, to examine the influence of the inhibitor on the corrosion process. The combination of SEM imaging and EDS analysis revealed differences in surface morphology and elemental distribution, shedding light on the formation of corrosion products and the presence of inhibitor layers. Additionally, the AFM system employed in this study was the Asylum Research MFP-3D, a high-precision instrument produced by Oxford Instruments.

To investigate the chemical properties of the DMTS inhibitor, we used the ATR-FTIR technique, with a spectral range from 4000 to 400 cm^{-1}, which allowed us to identify functional groups and monitor chemical interactions on the metal surface. The crystal structure of the metal's surface was also characterized using X-ray Diffraction (XRD). This method provides insight into the phase composition and structural changes in the metal due to corrosion.

This integrated approach, combining microscopy, elemental analysis, and spectroscopy, offers a comprehensive understanding of the corrosion process and the efficacy of the DMTS inhibitor. By comparing samples with and without the inhibitor, we can assess the protection mechanisms and identify key elements and structural changes associated with corrosion resistance in hydrochloric acid.

2.4. Molecular modeling

2.4.1. DFT computations

Correlation analysis was conducted to compare the experimentally determined corrosion inhibition efficiencies with various quantum chemical descriptors of the inhibitor molecule, utilizing theoretical calculations [42–44]. The DFT calculations utilized the B3LYP functional along with the 6-311G (d, p) basis set, executed using Gaussian 09W [45] and Gaussview software [46]. This particular basis set was chosen for the DMTS molecule because of its proven effectiveness in accurately depicting molecular orbitals while ensuring computational efficiency, which is critical for smaller, localized organic molecules. Furthermore, we explored quantum chemical parameters to deepen our

understanding of the interactions between the XC38 steel and the DMTS inhibitor. These parameters include E_{HOMO} (Highest Occupied Molecular Orbital Energy), E_{LUMO} (Lowest Unoccupied Molecular Orbital Energy), E_g (Energy Gap), electronegativity (χ), hardness (η), softness (σ), and electrophilicity index (ω). These parameters were calculated using the following mathematical relationships, providing insights into the electronic structure and reactivity of DMTS inhibitor [44,47–50]:

$$I = -E_{HOMO} \tag{5}$$

$$A = -E_{LUMO} \tag{6}$$

$$\Delta E_{Gap} = E_{LUMO} - E_{HOMO} \tag{7}$$

$$\chi = \frac{I + A}{2} \tag{8}$$

$$\eta = \frac{I - A}{2} \tag{9}$$

$$\sigma = \frac{1}{\eta} \tag{10}$$

$$\omega = \frac{\chi^2}{2\eta} \tag{11}$$

To gain deeper insights into the properties and interactions of the DMTS inhibitor, particularly its engagement with the steel substrate modeled by a metal cluster (Fe_{60}), a specialized computational approach was necessary due to the system's complexity and size [51,52]. The def-SV(P) basis set was employed for its proficiency in managing extensive electron interactions within large metal clusters, paired with the M06-2X functional [53,54], recognized for its precise handling of non-covalent interactions. These calculations were performed within the Turbomole 7.4 software environment [55–60], facilitating a refined and accurate optimization that closely replicates the inhibitor's interaction with the metal surface.

For the analysis of non-covalent interactions (NCI), the advanced technique of Reduced Density Gradient (RDG) was applied [61,62]. This analysis explored decreased density gradients and electron density (σ) to discern subtle forces such as hydrogen bonds, van der Waals forces, and steric repulsions [63–65]. The Multiwfn computational tool [66] further examined these subtle systemic interactions. The results were visually represented through Electrostatic Potential (ESP) and Electron Localization Function (ELF) maps, along with RDG plots, using the Visual Molecular Dynamics (VMD) interface [67]. Additionally, gnuplot was employed to create color scatter plots for detailed visualization [68].

2.4.2. Monte Carlo (MC) simulations

In our study, Materials Studio 2017™, a powerful computational tool referenced in works by [69], was employed to perform Metropolis Monte Carlo (MC) simulations by applying its Adsorption module [50, 70]. These simulations aimed to investigate the inhibition mechanisms of DMTS on steel surfaces. The MC simulations method is particularly effective for identifying the most favorable adsorbate/adsorbent combinations in terms of available energy, a critical factor in understanding the adsorption efficiency of corrosion inhibitors. In our simulations, we specifically focused on modeling the adsorption behavior of DMTS on steel surfaces. This involved setting up simulation boxes whose dimensions were determined based on the number and type of molecules being simulated, ensuring an accurate representation of the physical system. The interaction forces between the DMTS molecules and the steel surface were computed during the simulation. This was accomplished by employing the "Dreiding" force field, a versatile and widely accepted method for modeling molecular interactions [65,71–73]. The choice of the Dreiding force field was instrumental in accurately capturing the complex interactions that occur during the adsorption process, thus providing vital insights into the inhibitory action of DMTS

at a molecular level.

These advanced computational methodologies enabled a thorough exploration of the interactions within the molecular system, providing valuable insights into the molecular mechanisms underpinning the inhibitory efficacy of the DMTS molecule.

3. Results and discussion

3.1. FTIR spectroscopy analysis

The FTIR analysis was crucial in identifying the functional groups in DMTS. Our study analyzed the FTIR spectra of DMTS, which spanned a frequency range from 400 to 4000 cm^{-1}, as shown in Fig. 1 (a). The spectral data provided valuable insights into the molecular structure of DMTS, revealing various functional groups through their characteristic absorption peaks. As previously reported, a prominent absorption peak at 3349 cm^{-1} was observed, indicative of the -NH bond, suggesting the presence of amine compounds in DMTS [74]. Another significant peak at 3175 cm^{-1} corresponded to the -NH$_2$ bond. The absorption peaks at 1692 and 1621 cm^{-1} were attributed to the (C=O) and (C=N) amide I bond, respectively. These peaks are critical in identifying the amide functionality within the DMTS structure.

Additionally, the band observed at 1502 cm^{-1} was linked to the stretching vibrations of the C=C bonds, characteristic of aromatic rings in the DMTS molecule. The absorption band at 1455 cm^{-1} indicated the presence of C—N bonds. Further, the band at 1267.68 cm^{-1} was related to the C—N amide III bonds, highlighting the complexity of the DMTS structure. An absorption band at 1137 cm^{-1} confirmed the presence of a triazole (N-N) bond, while the band at 1019 cm^{-1} was attributed to the vibrations of the C=S bond, a key feature in the thiosemicarbazone group. Lastly, peaks at 747 and 630.64 cm^{-1} were identified, indicating the presence of the (-C—H) bond and the furan ring, respectively [74]. These FTIR findings are essential as they confirm the successful synthesis of DMTS and provide a detailed understanding of its chemical structure, which is crucial for comprehending its function as a corrosion inhibitor.

3.2. XRD analysis

The XRD analysis conducted on DMTS provided crucial insights into its crystalline structure. As confirmed by the XRD patterns, DMTS exhibits a nanocrystalline arrangement, with prominent peaks at 16.48° and 24.28°, a finding aligned with the study carried out by Boukerche et al. [36]. However, the overall structure of DMTS is predominantly polycrystalline, as evidenced in the XRD pattern presented in Fig. 1 (b). This polycrystalline nature of DMTS is significant, as it suggests a complex and varied crystalline structure. The detailed structural study highlights that the specific arrangement of the nanocrystals within DMTS is influenced by the compound's molecular structure and the conditions under which it was synthesized. Such elements are crucial when choosing the final crystalline structure of the compound. The XRD pattern in Fig. 1 (b) reinforces the polycrystalline nature of DMTS and provides valuable information about the material's structural behaviors, growth processes, electrical transport, and optical characteristics. These aspects are particularly important for understanding the functional properties of DMTS, especially in its application as a corrosion inhibitor.

Furthermore, the XRD analysis revealed a preferred crystallite orientation even during the initial stages of molecule formation. This observation suggests that the crystallization process of DMTS begins early in its formation, leading to a distinct and characteristic crystalline orientation. Such insights gained from XRD analysis are invaluable for comprehending the material properties of DMTS and how these properties may influence its effectiveness in practical applications. The Debye-Scherrer equation was utilized to estimate the mean crystallite size (D).
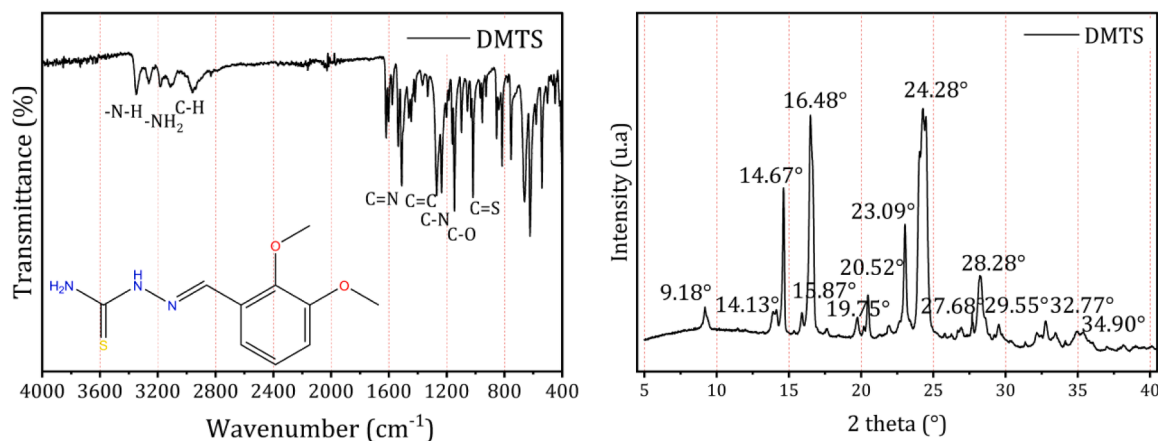
Fig. 1. (a) FTIR spectrum and (b) XRD pattern of DMTS (the inhibitor).

Table 2
Crystallite size of the synthesized DMTS inhibitor.

N°	2θ (°)	B (Radians)	D (A°)	D (nm)	D_{moy} (nm)
1	9.003	0.204	7.131	0.713	23.97
2	14.633	0.003	556.177	55.618	
3	16.544	0.006	261.514	26.151	
4	20.519	0.416	3.536	0.354	
5	20.519	0.003	460.075	46.007	
6	23.047	0.004	371.481	37.148	
7	24.296	0.011	139.293	13.929	
8	28.262	0.008	195.618	19.562	
9	29.541	0.004	400.712	40.071	
10	39.183	0.822	1.870	0.187	

$$D = \frac{k\lambda}{\beta\cos\theta} \tag{12}$$

In the context of the XRD analysis for DMTS, the Scherrer equation is also employed to calculate the size of the crystallites. This equation is a critical tool for understanding the crystalline nature of materials studied through XRD. The Scherrer constant, k, is set at 0.94 and is typically used for spherical crystallites exhibiting cubic symmetry. The equation also incorporates the angular full-width at half-maximum (β) of the XRD peak, measured in radians. This measurement is crucial as it reflects the broadening of the diffraction peak due to the finite size of the crystallites. The Bragg diffraction angle (θ) is another essential parameter in the equation, which in this instance is 12.14708∘. This angle represents the specific position where the maximum diffraction intensity is observed, corresponding to the lattice planes of the crystallites.

Moreover, the incident X-ray beam (λ)'s wavelength is a standard reference point for calculating the sample's spacing between the crystalline planes. By applying the Scherrer equation with these parameters, the crystallite sizes corresponding to different peaks in the XRD pattern of DMTS can be accurately determined. These sizes are essential for understanding the material's structural properties, as they provide insights into the nanoscale arrangement of the crystallites within the sample. The calculated crystallite sizes for the various peaks observed in the XRD pattern of DMTS are detailed in Table 2 of the study. Thus, this data is vital for correlating the structural properties of DMTS with its functional performance, particularly in applications such as corrosion inhibition. One typical parameter value, D = 12.98 nm, was determined using the standard method for structural analysis.

3.3. NMR analysis

The nuclear magnetic resonance (NMR) spectroscopy results for DMTS provide detailed insights into its molecular structure. In the proton (^{1}H) NMR spectrum, as shown in Fig. 3, a range of characteristic peaks can be observed, each corresponding to different protons in the DMTS molecule. A singlet at approximately 9.5 ppm is noticed, corresponding to the proton attached to the nitrogen atom. This peak indicates the presence of an amine or similar nitrogen-bearing functional group. Another notable singlet, found around 6.3 ppm, resonates for the two protons of the second nitrogen atom. This is consistent with the chemical environment expected in a molecule like DMTS. A singlet represents the proton linked to the imine carbon at around 7.7 ppm. The imine functional group is a key feature in thiosemicarbazone compounds. The aromatic ring's three protons appear at 7 to 7.6 ppm. This range is typical for protons on an aromatic ring and helps confirm the aromatic nature of the compound.

The six protons of the two methoxy groups resonate around 3.8-3.9 ppm. This aligns with the expected chemical shift for methoxy protons, as noted in previous research [75,76]. In the carbon-13 (^{13}C) NMR spectrum, presented in Fig. 4, various signals correspond to the different carbon atoms within the DMTS structure: Signals at δ 151.75 and 149.54 ppm were assigned to the CH═N and C═S functional groups, respectively. These peaks are indicative of the imine and thiosemicarbazide moieties in DMTS. The aromatic carbon signals were detected in the δ 108.41–125.72 ppm range, typical for carbons in an aromatic ring structure. A signal at δ 56.03 ppm corresponds to the carbon atoms of the methoxy groups. This is consistent with the chemical shift expected
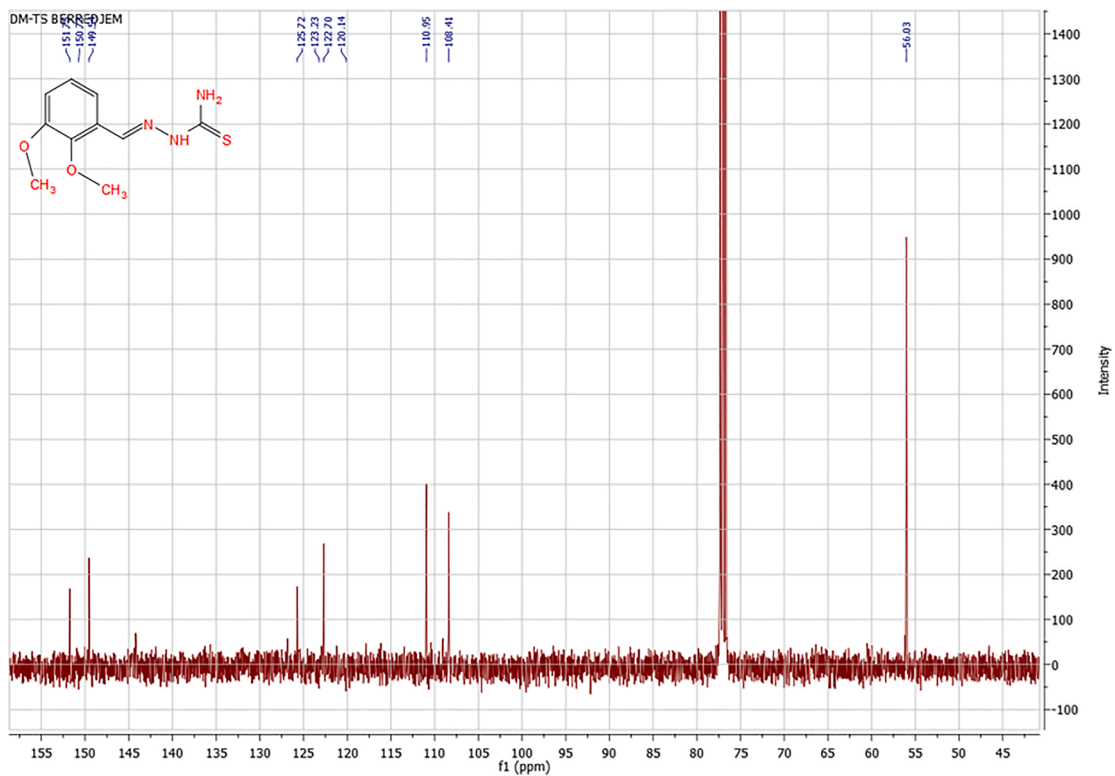
(a)

(b)
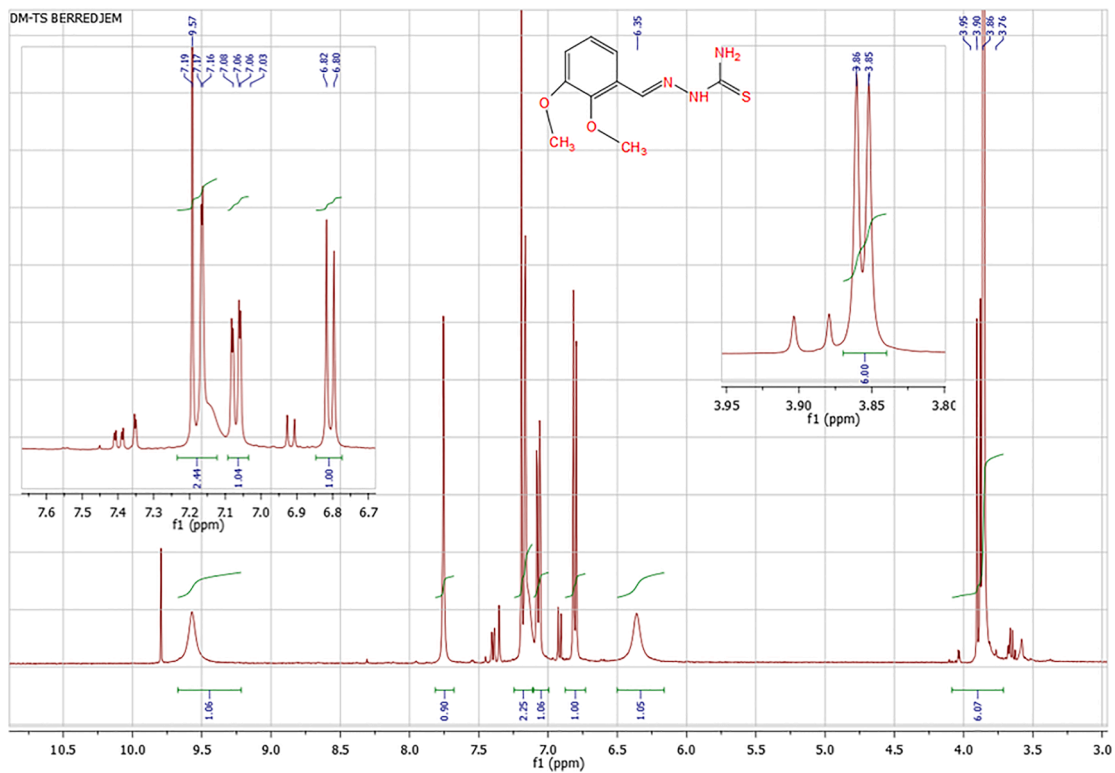
Fig. 2. (a) H^{1}NMR and (b) ^{13}C NMR of the spectrum of DMTS compound.
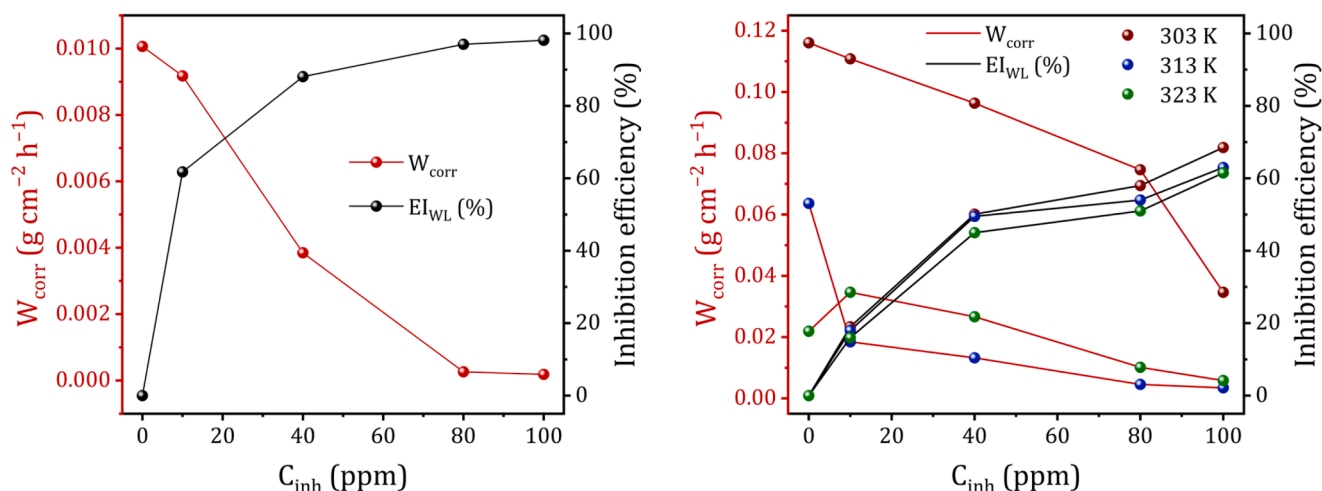
Fig. 3. Efficiency and inhibitory corrosion rate of XC38 steel over time in a 1 M HCl solution as an effect of concentration (a) and temperature (b).
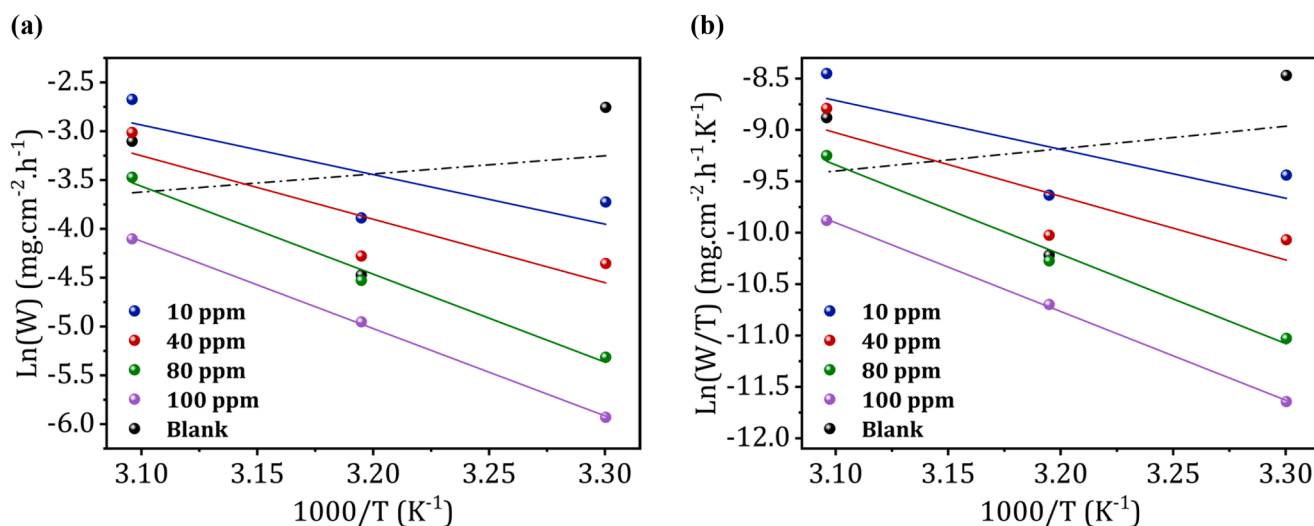

Fig. 4. The relation between a) ln W_{corr} and b) ln(W_{corr}/T) vs. $1/T$ for XC38 in 1 M HCl solutions containing DMTS inhibitor at different concentrations.

Table 3
Corrosion data for XC38 carbon steel in an acidic media as a function of DMTS concentration after immersion of 24 h.

C (ppm)	Δ_m (g)	W (g.cm^{-2}.h^{-1})	θ	EI_{WL}(%)
Blank	0.4266	1.0063×10^{-2}	/	/
10 ppm	0.3890	9.1766×10^{-3}	0.6178	61.78
40 ppm	0.1630	3.8452×10^{-3}	0.8808	88.08
80 ppm	0.0111	2.6185×10^{-4}	0.9703	97.03
100 ppm	0.0079	1.8636×10^{-4}	0.9814	**98.14**

Table 4
Corrosion data for XC38 carbon steel in an acidic media as a function of DMTS temperature after immersion of 2 h.

C_{inh} (ppm)	Temperature(K)	Δ_m (g)	W (g.cm^{-2}.h^{-1})	θ	EI_{WL}(%)
Blank	**303**	0.0794	0.06363	-	-
10 ppm		0.01232	0.01845	0.19	19.00
40 ppm		0.0868	0.01324	0.501	50.10
80 ppm		0.0549	0.00455	0.58	58.00
100 ppm		0.0292	0.00345	0.685	68.50
Blank	**313**	0.1906	0.02193	-	-
10 ppm		0.1224	0.03464	0.18	18.00
40 ppm		0.0941	0.02663	0.495	49.50
80 ppm		0.0359	0.01016	0.54	54.00
100 ppm		0.0205	0.0058	0.63	63.00
Blank	**323**	0.3554	0.11606	-	-
10 ppm		18,409	0.11080	0.16	16.00
40 ppm		15,298	0.09633	0.45	45.00
80 ppm		0.9158	0.07462	0.51	51.00
100 ppm		0.5298	0.03464	0.615	61.50

for such groups in an organic compound.

These NMR findings, as corroborated by Boulechfar et al. [77], are critical for validating the proposed structure of DMTS. They provide a detailed and nuanced understanding of its molecular composition, which is crucial for studies on its properties and potential applications, such as in corrosion inhibition.

3.4. Evaluation of weight loss

3.4.1. Concentration effect

Gravimetric analysis, a foundation stone in corrosion science, is a pivotal method for evaluating the extent of material degradation due to

corrosive processes. By measuring the mass loss of a specimen over time, this technique quantitatively reveals the metal's resilience or vulnerability to corrosion, as well as the efficacy of potential inhibitors. In evaluating the anti-corrosive capabilities of DMTS inhibitor for XC38

carbon steel, we quantified the inhibition efficiency ($IE_{WL}\%$), weight loss (Δ_m), and surface coverage (θ) through gravimetric assessments after a 24-hour immersion in a 1 M HCl solution. These metrics, summarized in Table 3, provide insight into the performance of DMTS at varying concentrations.

A notable trend depicted in Fig. 3 (a) illustrates that the corrosive attack on XC38 steel diminishes substantially with the incremental addition of DMTS, culminating in a substantial decrease in corrosion rates. The data reveal a significant enhancement in protection with 100 ppm DMTS, yielding an $IE_{WL}\%$ of 98.14 %. Even at a minimal inhibitor concentration of 10 ppm, the steel demonstrates a marked resistance to the acidic environment, as evidenced by an inhibition efficiency of 61.78 %.7

3.4.2. Temperature effect

Gravimetric experiments were conducted at 303, 313, and 323 K. The temperature change is a key indicator used to identify the inhibition performance of the DMTS inhibitor at different concentrations (Fig. 3 (b)). Consequently, the gravimetric outcomes elucidate that DMTS is an efficacious corrosion inhibitor, with the observed variation in electrochemical parameters suggesting a progressive establishment of a protective barrier.

Mass loss and corrosion rate reduction corresponded with an increase in DMTS concentration. This inverse relationship may be attributed to the enhanced coverage of the steel surface by the inhibitor molecules, resulting in a pronounced molecular barrier that mitigates corrosion. Such coverage likely stems from a significant rate of molecular adsorption, as indicated by the increased θ with higher concentrations of DMTS. These findings are further validated by the electrochemical data presented in Table 4, reinforcing DMTS's role as a potent inhibitor in preserving metal in corrosive environments.

3.5. Activation thermodynamics

The temperature dependence of molecular adsorption and desorption mechanisms plays a pivotal role in corrosion dynamics [78]. To quantify the energy barriers associated with corrosion processes, the Arrhenius equation is employed:

$$W_{corr} = A\exp\left(\frac{-E_a}{RT}\right) \quad (13)$$

Where E_a signifies the activation energy, A is the Arrhenius pre-exponential factor, T is the thermodynamic temperature, R is the universal gas constant, and W_{corr} denotes the rate of corrosion. As depicted in Fig. 4 (a), we constructed an Arrhenius plot to graphically ascertain E_a for XC38 carbon steel in 1 M HCl by correlating ln W_{corr} with $1000/T$. The estimated activation energies, derived from the linear regressions of these plots, are tabulated in Table 5.

Advancing our understanding, the standard enthalpy (ΔH_a^0) and entropy (ΔHS_a^0) of activation are determined using the modified Arrhenius expression:

$$W_{corr} = \frac{RT}{Nh}\exp\left(\frac{\Delta S_a^0}{R}\right)\exp\left(\frac{-\Delta H_a^0}{RT}\right) \quad (14)$$

Where h and N represent Planck's constant and Avogadro's number,

respectively. This modified expression facilitates the extrapolation of thermodynamic parameters from a plot of ln W_{corr}/T versus $1000/T$, illustrated in Fig. 4 (b), with the slope and intercept corresponding to $-\Delta H_a^0/RT$ and $R/Nh + \Delta S_a^*/R$, respectively. The thermodynamic findings suggest that the dissolution process of carbon steel is endothermic, reflecting a complex formation that is associative, indicating a decrease in system disorder transitioning from reactants to the activated complex [79].

Detailed examination of Table 5 reveals that the activation energy increases from -15.471 kJ·mol^{-1} in the absence of inhibitors to 42.173 kJ·mol^{-1} upon the introduction of 10 ppm DMTS, signaling the physisorptive interactions of DMTS molecules with the XC38 steel surface [44,80]. This indicates a reduction in corrosion rates attributed to the inhibitory shield provided by DMTS adsorption, which impedes both anodic and cathodic reactions, leading to a decelerated corrosion process on the protected metal surface [47,73].

As the concentration of DMTS increases, the increment in E_a values refers to the geometric obstruction by adsorbed inhibitory molecules on the metal interface. The calculated negative values of ΔH_a^0 reinforce the exothermic disposition of steel dissolution, while the substantial negative magnitude of ΔHS_a^0 reaffirms the associative characteristic of the activated complex, underlining a transformation that leads to reduced disorder within the system [47,81].

3.6. Adsorption isotherm

Understanding molecular interactions between inhibitory compounds and metal surfaces is fundamental to corrosion control, a concept that can be analyzed through adsorption isotherms [47]. Such isotherms provide valuable insights into the nature and extent of electrochemical interactions during the adsorption of organic molecules on metallic substrates. This study aims to elucidate the governing adsorption isotherm by fitting experimental data to classic models, including Langmuir, Temkin, and Freundlich, each based on different assumptions regarding surface homogeneity and adsorbate interactions [50,82].

The Langmuir isotherm posits a homogeneous adsorption plane with discrete, energetically equivalent sites, each accommodating a single adsorbate molecule, and presumes no adsorbate-adsorbate interactions [49,50,83]. This model is quantitatively expressed as:

$$\frac{C_{inh}}{\theta} = \frac{1}{K_{ads}} + C_{inh} \quad (15)$$

Conversely, the Temkin isotherm acknowledges a decline in adsorption energy correlating with surface coverage and is described by:
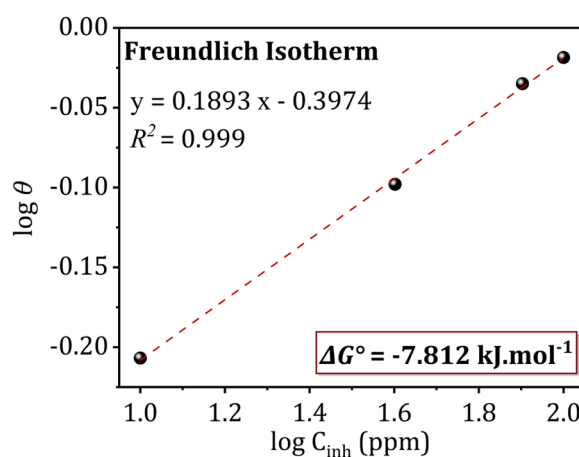
$$\exp(-2\alpha\theta) = K_{ads}C_{inh} \quad (16)$$

Table 5
Activation parameters for XC38 in 1 M HCl with different concentrations of DMTS.

C_{inh} (ppm)	E_a (J mol^{-1})	ΔH_a^0 (J mol^{-1})	ΔS_a^0 (J mol^{-1} K^{-1})
Blank	−15.471	18.071	−331.716
10 ppm	42.173	−39.573	−147.307
40 ppm	54.037	−51.437	−113.143
80 ppm	74.849	−72.249	−51.227
100 ppm	74.354	−71.754	−57.442

Fig. 5. Freundlich Isotherm adsorption for XC38 in 1 M HCl at different concentrations of DMTS.
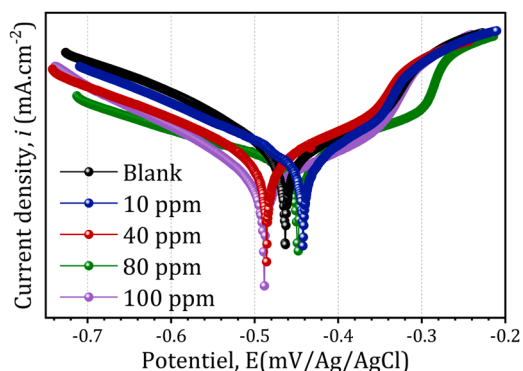
Fig. 6. Steel polarization curves in 1 M HCl solution without and with varying concentrations of DMTS.

Table 6
The impact of the DMTS's inhibitor concentration on XC38 properties in 1 M HCl.

C_{inh} (ppm)	i_{corr} (μA/cm^2)	E_{corr} (V)	β_a (mv/des)	β_c (mv/des)	E_{PDP} (%)
HCl (Blanc)	139.5	−0.441	68.5	−109	-
10 ppm	84	−0.462	73	−96	40.0
40 ppm	80	−0.485	67	−70	42.0
80 ppm	11.7	−0.444	51.7	−85	91.6
100 ppm	8.4	−0.487	55.2	−62.7	**94.0**

Here, K_{ads} is the adsorption equilibrium constant, and α signifies the adsorbate interaction parameter.

The Freundlich isotherm, on the other hand, accommodates surface heterogeneity and adsorbate interactions, offering insight into the non-uniform distribution of adsorption energies across the surface, encapsulated in the equation:

$$log\ \theta = log\ K_{ads} + \alpha\ log\ C_{inh} \qquad (17)$$

The experimental data converged optimally with the Freundlich isotherm model, achieving a correlation coefficient (R^2) of 0.999, indicating a heterogeneous surface with variable adsorption potentials, as illustrated in Fig. 5.

The spontaneity of the adsorption process is confirmed by the negative values of the standard free energy of adsorption (ΔG°_{ads}). Specifically, a ΔG°_{ads} value of − 7.812 kJ mol^{-1} indicates a physisorptive interaction characterized by electrostatic forces rather than charge sharing typical of chemisorption [84]. The adsorption constants derived from the Freundlich model allow the computation of ΔG°_{ads} using the following relation:

$$\Delta G^{\circ}_{ads} = -RT\ln(55.5 \times K_{ads}) \qquad (18)$$

Given that R is the universal gas constant, 55.5 represents the molar concentration of water, T is the absolute temperature, and K_{ads} the adsorption equilibrium constant.

The Freundlich isotherm model provided the best fit for the adsorption of DMTS on XC38 steel, and the negative ΔG°_{ads} value confirms that the adsorption of DMTS on the XC38 carbon steel surface is a spontaneous process, consistent with physical adsorption mechanisms. This physisorption is indicative of weak van der Waals forces and hydrogen bonding between the DMTS molecules and the steel substrate [85]. Consequently, these findings support the effectiveness of DMTS as a corrosion inhibitor through the formation of a stable and durable protective barrier on the steel surface.
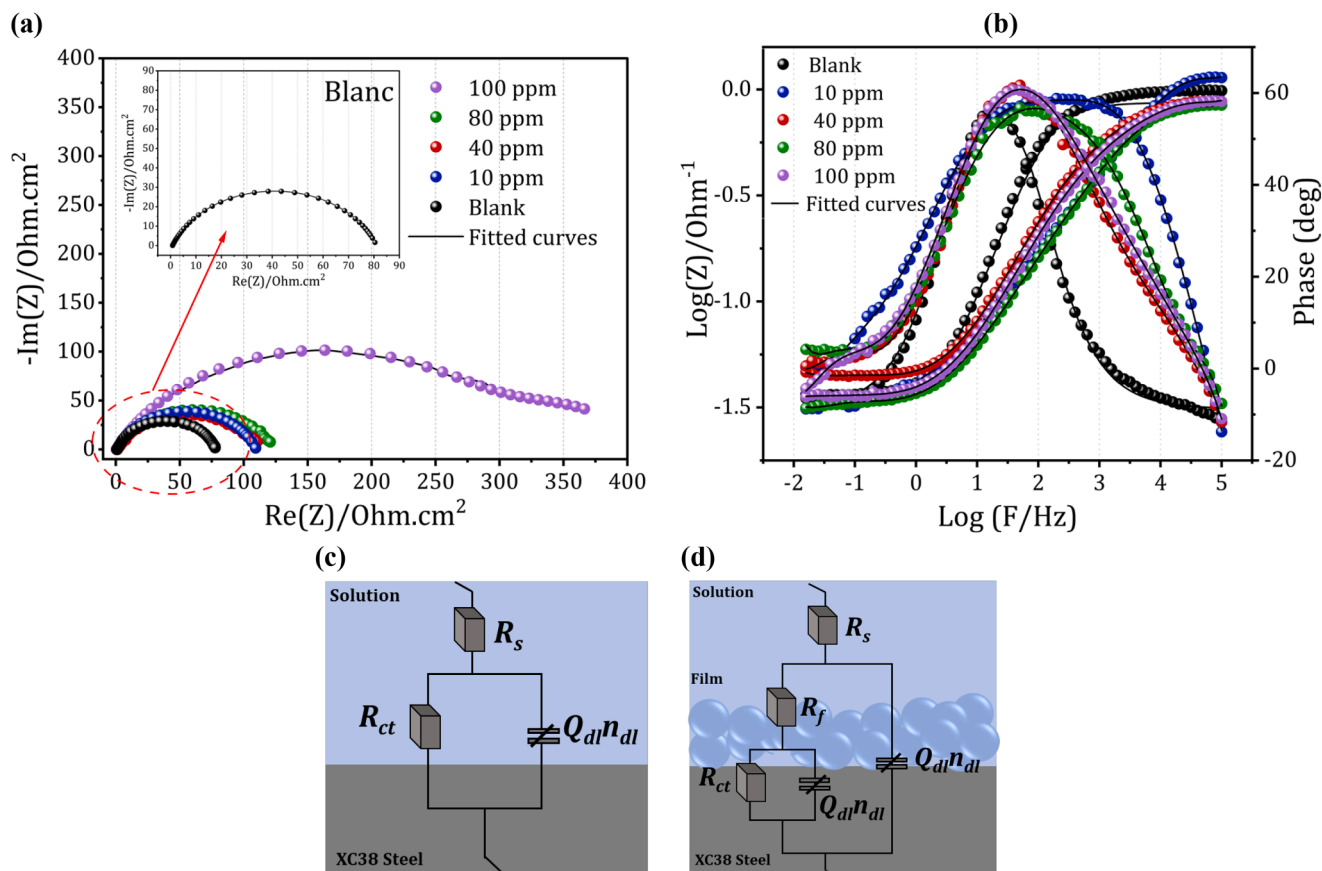

Fig. 7. The impact of inhibitor concentration on carbon steel in 1M HCl Solution: (a) Nyquist plots (b) Bode plots, and Electrical circuit equivalent to fitting EIS data, (c) solution without inhibitor (Blank), and (d) solution with inhibitor.

3.7. PDP measurements

PDP measurements, performed in a 1 M HCl solution at 25 °C with varying concentrations of DMTS (0 to 100 ppm), offer insights into the corrosion behavior of XC38 steel under acidic conditions [86]. The results, depicted in Fig. 6 and detailed in Table 6, highlight the significant impact of DMTS on corrosion parameters, including current densities, potential, and polarization resistances. The polarization curves (Fig. 6) demonstrate a noticeable reduction in current density with increasing concentrations of DMTS, inversely correlating with the steel's corrosion rate. Specifically, the corrosion current density (i_{corr}) markedly decreases from 139.5 $\mu A/cm^2$ in the blank solution to just 8.4 $\mu A/cm^2$ at 100 ppm of DMTS, illustrating the inhibitor's potent effect. The corrosion potential (E_{corr}) shows slight shifts, indicating that the inhibitor predominantly influences the kinetics rather than the thermodynamics of the corrosion process.

Further analysis of Tafel slopes (β_a and β_c) from Table 6 reveals an increase in polarization resistance, especially notable at higher DMTS concentrations. This suggests a more effective barrier formation on the metal surface, enhancing protection. Remarkably, the inhibition efficiency (E_{PDP}) reaches up to 94 % at 100 ppm, underscoring the high effectiveness of DMTS in this environment. This trend of increased inhibitory effectiveness with higher concentrations of DMTS implies a proportional increase in the adsorption of inhibitor molecules on the steel surface, thereby forming a robust protective layer that impedes both anodic dissolution and cathodic reduction processes. The consistent corrosion potential across varying concentrations further indicates that DMTS stabilizes the corrosion potential, maintaining a steady state favorable for corrosion protection. Therefore, the PDP measurements confirm DMTS as a highly effective corrosion inhibitor for XC38 steel in acidic conditions, significantly reducing corrosion current density and enhancing corrosion resistance, making it an excellent choice for industrial applications where steel is exposed to corrosive acidic environments.

3.8. EIS measurements

The electrochemical characteristics of the samples were analyzed using the EIS method. Fig. 7 (a) and (b) show the Nyquist and Bode curves for various concentrations of DMTS (inhibitor) in 1M hydrochloric acid medium. EIS measurements, when conducted at the corrosion potential (E_{corr}), provide critical kinetic parameters that define the corrosion characteristics of steel as well as the mechanism of action of the inhibitor [87].

Established metrics for assessing overall corrosion resistance include the Nyquist diameter and impedance at the minimum frequency (0.01 Hz) [88]. The results of these tests indicate that the DMTS inhibitor offers optimal corrosion protection at a concentration of 100 ppm, as shown by the largest Nyquist diameter and the lowest impedance at the lowest frequency. In contrast, the corrosion resistance measurements for the blank solution are the lowest.

A commonly used method for quantifying EIS data involves models representing electrochemical equivalent circuits (EECs) [89]. A solitary peak is visible in the null solution's Bode-phase angle curves. The inhibitor, on the other hand, increases the probability of a two-time
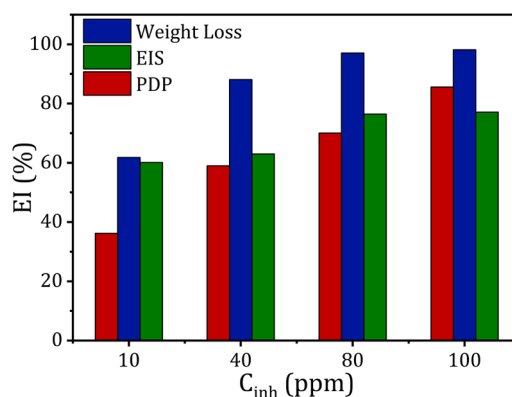

Fig. 8. Inhibitory efficiency obtained by weight loss, polarization (PDP), and impedance (EIS) methods for different concentrations of DMTS.

constant EEC. A two-time constant EEC was implemented to mimic the EIS data for changing inhibitor concentrations, whereas a one-time constant EEC was used to represent the blank solution. Using analogous circuits documented in the scientific literature, we assessed the EIS data about carbon steel inhibition by organic chemicals in an acidic solution.

As seen in Fig. 7, two distinct equivalent electrical circuit (EEC) models corresponded with the experimental EIS diagrams. These circuits are influenced by the solution resistance (R_s), the charge transfer resistance (R_{ct}) that exists between the working electrode and the solution interface, the double-layer capacitance (Q_{dl}), and the film resistance (R_f). Resistance to corrosion results from the gradual absorption of oxygen and electrolytes via the imperfections in the inhibitor coating [90].

The values of electrochemical parameters derived from simulations of impedance spectra with and without the addition of various amounts are shown in Table 7.

The Nyquist diagram analysis yielded the critical impedance parameters shown in Table 7. The values where R_{ct}^{inh} and R_{ct}^0 denote the capacity of inhibited and uncontrolled double-layer adsorption, respectively. A major improvement in corrosion behavior is shown by the increased resistance (R_{ct}) as the concentration of the inhibitor rises. Ultimately, this increased resistance leads to a more effective method of corrosion prevention [77].

Fig. 8 illustrates the variation in inhibitory efficiency determined by three distinct methods—electrochemical impedance spectroscopy, gravimetry, and polarization curves—concerning the concentration of the DMTS compound in 1 M HCl medium. We observe congruence between the values obtained via electrochemical measurements and those determined using gravimetry.

3.9. Surface and morphology investigations

3.9.1. SEM analysis

Fig. 9 (a) presents the pristine surface of XC38 steel before any experimental treatment, showing a smooth and unblemished morphology typical of polished steel surfaces. Upon exposure to a 1 M HCl solution without any inhibitor, as depicted in Fig. 9 (b), the surface

Table 7

XC38 carbon steel electrochemical impedance parameters in 1M Hydrochloric acid with varying DMTS inhibitor doses.

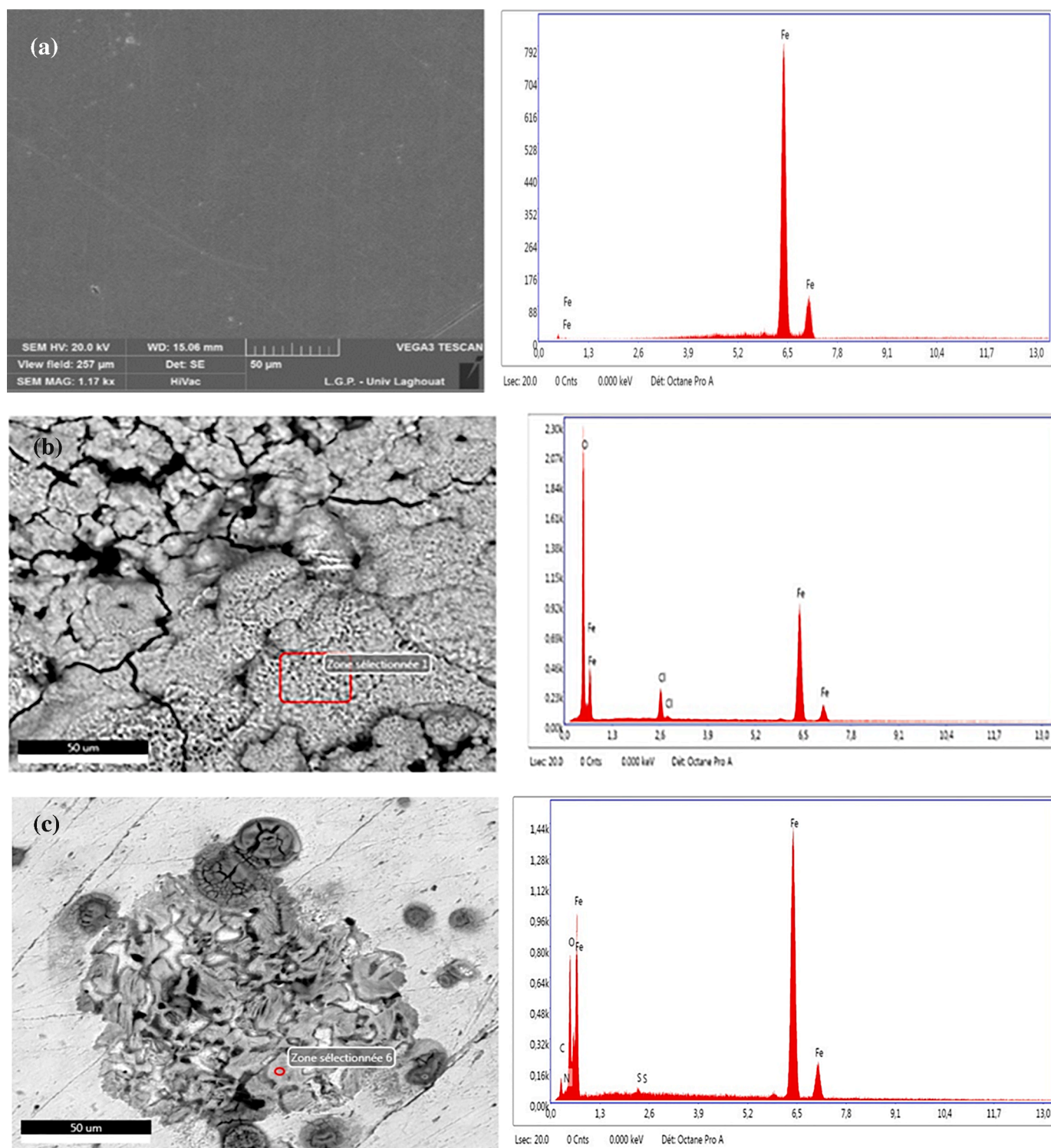| C (ppm)	R_S ($\Omega.cm^2$)	R_f ($\Omega.cm^2$)	Q_f ($\mu F.cm^{-2}$)	R_{ct} ($\Omega.cm^2$)	Q_{dl} ($\mu F.cm^{-2}$)	R_{tot} ($\Omega.cm^2$)	E%
Blanc	0.81	/	112	26.7	/	80	/
10 ppm	0.8	69	847	8	57	110	65.32
40 ppm	0.78	90	91	24	1100	113	76.57
80 ppm	0.80	123	860	3	10	126	78.80
100 ppm	0.5	313	567	100	3500	413	**93.53**

Fig. 9. Images from the 50 μm-SEM of polished XC38 steel samples (a), after 72 h immersion in 1 M HCl solution: without inhibitor (b) and with 100 ppm inhibitor (c).

integrity of the steel significantly deteriorates. This condition is evidenced by the formation of gray clusters and notable pitting, indicative of severe corrosive attack. These morphological changes represent the formation of iron oxide, suggesting widespread corrosion across the entire surface [91]. In contrast, Fig. 9 (c) illustrates the surface of XC38 steel after immersion in a solution of 1 M HCl containing 100 ppm DMTS. Remarkably, the surface appears almost untouched by corrosion, maintaining a smoothness comparable to the untreated sample. This

stark difference underscores the effectiveness of the DMTS inhibitor in protecting the steel by forming a protective coating that significantly restricts electrolyte access to the metal surface. The EDS spectra further support these findings. In the absence of the inhibitor, the oxygen peak in the EDS spectrum confirms the formation of iron oxide due to corrosion processes in the acidic medium.

Additionally, the presence of chloride ions on the surface after 72 h of exposure corroborates their role in facilitating pitting corrosion of the

Table 8
Different percentages of phases obtained by EDS measurements.

Element	XC38	XC38 + HCl	XC38 + HCl +Inhibitor		
Fe	100	55.98	49.56	47.78	42.65
O	-	39.58	25.26	29.88	32.51
C	-	-	22.04	18.47	20.50
Cl	-	4.44	-	-	-
N	-	-	2.84	3.50	3.47
S	-	-	0.30	0.37	0.87

carbon steel. Conversely, the EDS analysis of the steel surface treated with DMTS, as shown in Fig. 9 (c) and quantified in Table 8, reveals the presence of nitrogen and sulfur peaks. These elements indicate the successful adsorption of DMTS onto the steel surface, highlighting its role in providing effective corrosion protection.

The SEM examinations qualitatively show a significant retention of surface integrity in the DMTS-treated samples compared to those exposed to HCl alone. The observed film formed by the inhibitor on the steel surface is uniform and comprehensive, with very small infiltration channels, only a few micrometers in width, detected within the coating. These channels are critical for maintaining a continuous and well-adhered protective layer, thereby enhancing the overall corrosion resistance of the steel substrate. The comparative SEM and EDS analyses

provide compelling visual and chemical evidence of the protective efficacy of DMTS as a corrosion inhibitor for XC38 steel in acidic environments [92]. The inhibitor's ability to form a durable adsorbed layer on the steel surface effectively prevents the typical degradation seen in harsh acidic conditions, illustrating its potential for industrial applications where metal preservation is critical.

3.9.2. AFM analysis

AFM was employed to provide a detailed morphological analysis of XC38 steel surfaces exposed to corrosive conditions. This non-destructive technique was used to generate high-resolution images that help quantify the physical changes on the steel surface due to corrosion and evaluate the protective efficacy of the DMTS inhibitor. The steel samples were analyzed after 72 h of immersion in 1 M HCl, both with and without the addition of 100 ppm DMTS inhibitor, to understand the inhibitor's role in mitigating corrosion [93]. Fig. 10 depicts AFM scans from two sets of conditions: control samples before and after immersed in 1 M HCl (Fig. 10 (a) and (b)) and a test sample in 1 M HCl supplemented with 100 ppm DMTS ((Fig. 10 (c)). The control sample (Fig. 10 (a)) exhibited extensive surface damage characterized by deep pits and a high average roughness (R_a) of 83 nm, indicative of aggressive acid corrosion.

Conversely, the DMTS-treated sample (Fig. 10 (c)) showed a significantly smoother surface with a markedly reduced roughness. This
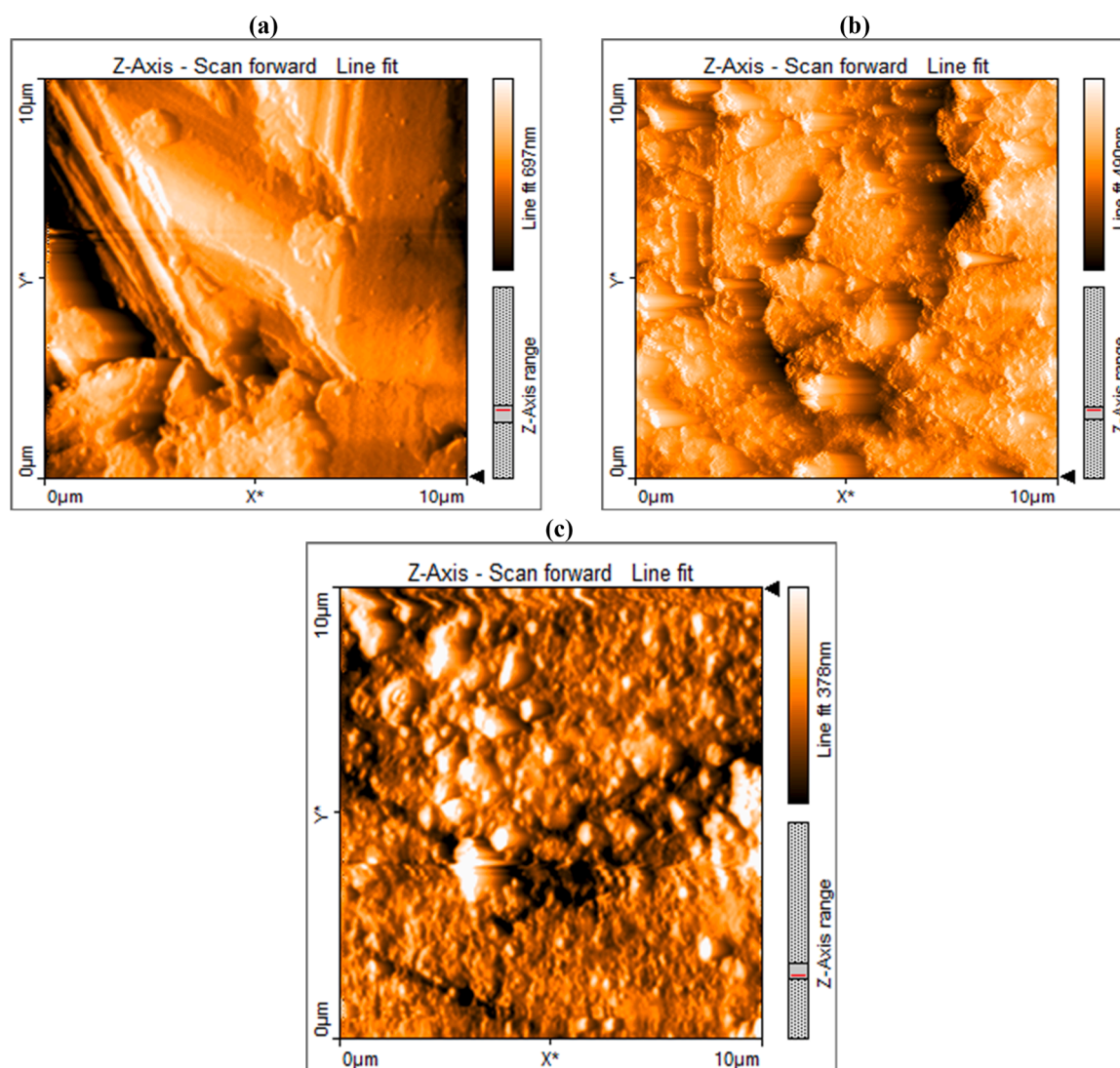

Fig. 10. AFM Morphological analysis of XC38 Steel surfaces before (a) and after 72 h in 1 M HCl solution without (b) and with DMTS inhibitor (c).
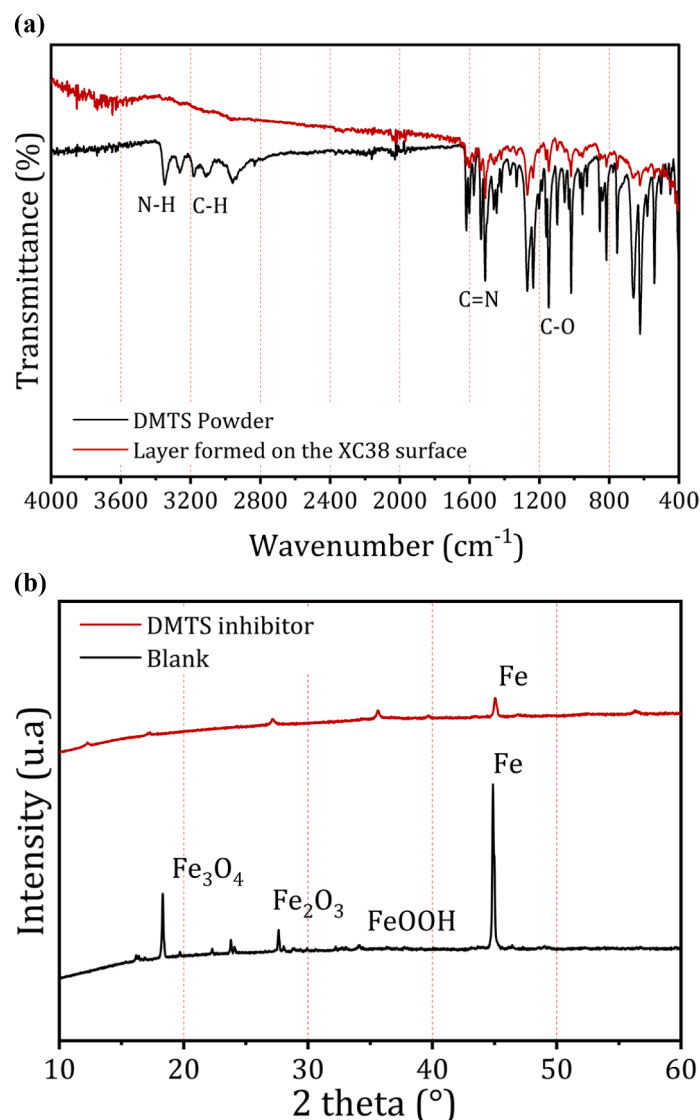
(a)

(b)

Fig. 11. ATR spectrum (a) and XRD patterns (b) of the XC38 surface after 24 h immersion in 1 M HCl solution containing 100 ppm of DMTS.

demonstrates the inhibitor's effectiveness in forming a protective barrier, which mitigates the acid's corrosive impact. Quantitative AFM data revealed a substantial decrease in surface roughness for the DMTS-treated steel, confirming the visual assessment. The smoother morphology of the treated sample suggests that DMTS successfully blocks active corrosion sites and possibly forms complexes with metal ions to preserve the steel's surface integrity. This analysis underscores DMTS's potential as an effective corrosion inhibitor for industrial applications where resistance to harsh acidic conditions is crucial [1,77, 80]. The protective properties of DMTS not only enhance the durability of metal components but suggest its broader applicability in managing corrosion-related challenges in industrial settings.

3.9.3. ATR-FTIR spectroscopy

ATR-FTIR spectroscopy is paramount for elucidating the molecular dynamics at the metal-inhibitor interface, providing a window into the subtleties of surface interactions [3,94]. This method is integral to confirming the adsorption of organic inhibitors, a cornerstone in corrosion mitigation. By interrogating the vibrational signatures of chemical bonds, ATR-FTIR analysis identifies functional groups and divulges the adsorptive behavior underpinning the inhibitor's performance.

ATR-FTIR spectroscopy was employed in this investigation to assess the surface interaction of XC38 steel with DMTS under corrosive conditions. Fig. 11 (a) unveils the spectral landscape of DMTS, distinguished by peaks representative of its molecular scaffold. Notable is the N-H bond's stretching vibrations observed between 3300–3500 cm^{-1}, which display a discernible shift, likely attributed to electron density modulation by adjacent sulfur. The aromatic C—H stretching frequencies manifest near 3000 cm^{-1}. Pertinently, the C=N stretch, a hallmark of the thiosemicarbazone genre, resonates around 1600 cm^{-1}, revealing a shift upon interaction with the metal surface, which suggests participation in complex formation with iron atoms. Additionally, the C—O stretching motions, typically between 1250-1000 cm^{-1}, underwent intensity variances, insinuating their role in surface bonding [1,44].

The spectral comparison clearly shows the inhibitor-induced modifications on the treated steel surface, which notably lacked the characteristic peaks of DMTS in isolation. The shifts and intensity changes in peak patterns are irrefutable spectroscopic fingerprints of DMTS adsorption on the XC38 steel, indicative of complexation and subsequent formation of a protective barrier against corrosion. These spectral insights complement the morphological and physical data obtained from SEM and AFM analyses, attaching a comprehensive understanding of the protective film's inhibition mechanism and genesis.
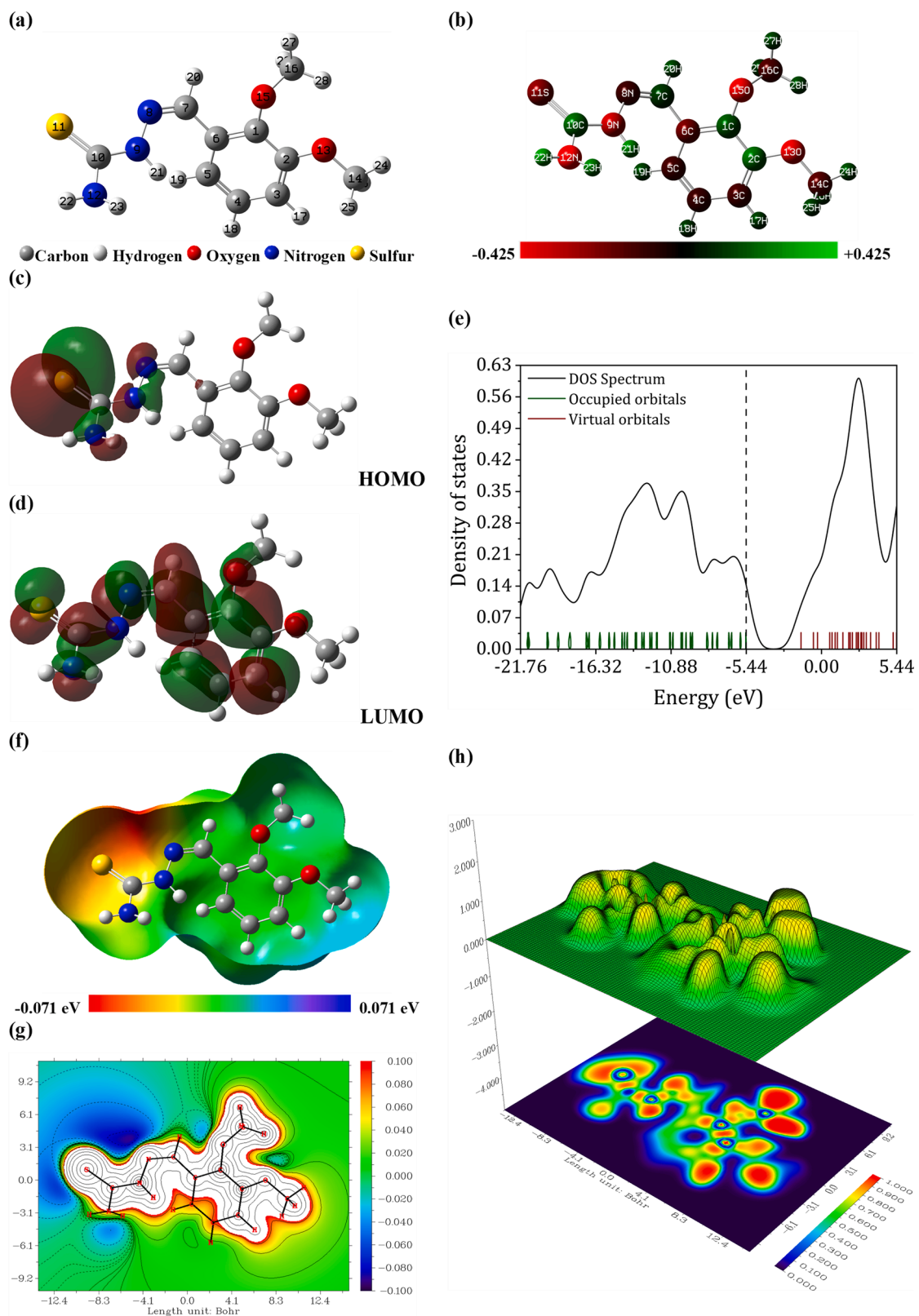
Fig. 12. The optimized geometry (a), the Mullikan atomic charge distribution (b), the HOMO (c), LUMO (d) orbitals, the total density of states (e), the electrostatic potential (f and g), and the ELF maps (h) at B₃LYB/6–311G(*d,p*) for DMTS inhibitor.

Table 9
The DFT calculated global reactivity parameters for DMTS compound.

E_t (eV)	μ (Debye)	E_{HOMO} (eV)	E_{LUMO} (eV)	E_g (eV)	χ (eV)	η (eV)	σ (eV)	ω (eV)
−1101.9288	9.3682	−5.4752	−1.4808	3.9944	3.4780	1.9972	0.2504	3.0284

3.9.4. Surface characterization through X-ray diffraction

XRD analysis yields critical insights into the surface chemistry alterations induced by corrosion and its mitigation through inhibitory action [95]. Fig. 11 (b) illustrates the diffraction patterns of XC38 carbon steel post a 24-hour immersion in 1 M HCl, both in the absence and presence of the DMTS inhibitor. In the uninhibited acidic environment, the steel surface exhibited characteristic peaks at 2θ values of 18.31° and 32.48°, corresponding to the formation of iron oxides, notably Fe_3O_4, Fe_2O_3, and FeOOH. These compounds are indicative of substantial oxidative degradation as a consequence of corrosive interaction with the chloride medium. Conversely, the inclusion of 100 ppm DMTS inhibitor markedly altered the XRD spectrum, revealing a prominent peak at 2θ = 45.52°, congruent with the crystalline structure of metallic iron. The peaks for iron oxides were absent, underscoring the inhibitor's role in staving off oxide formation. This phenomenon is attributed to the establishing of a protective adsorptive film by the DMTS molecules, effectively safeguarding the underlying metal surface. Therefore, this XRD assessment validates the efficacy of DMTS as a potent corrosion inhibitor, supplementing the empirical evidence gathered from other surface characterization techniques, including AFM, SEM, and ATR-FTIR spectroscopy.

3.10. Computational modeling analyses

3.10.1. DFT calculations

DFT was employed to elucidate the chemical reactivity of DMTS inhibitors, focusing on its potential as a corrosion inhibitor and its electronic and structural attributes. The molecular conformation, optimized using the B3LYP functional within the 6–311G (d, p) basis set framework, is depicted in Fig. 12 (a). DMTS, existing in a singlet state with a composition of 29 atoms, exhibits a total ground state energy (E_t) of −1101.9288 atomic units and a dipole moment (μ) of 9.3682 Debye, as recorded in Table 9. The heightened μ value may strongly indicate its inhibitory capabilities in conjunction with its role as a hydrogen bond donor [1,47,54,96,97]. Such a molecule, characterized by a substantial μ value, is expected to participate in various intermolecular forces, including dipole-dipole interactions, π-π stacking, and hydrogen bonding, facilitated by its polar nature and significant charge distribution. Mulliken charge distribution analysis on DMTS proves the molecule's significant charge disparity, as Fig. 12 (b) delineates. The chromatic gradient representing Mulliken charges across DMTS's 29 atoms uncovers an apparent polarity within its structure. Hydrogen atoms uniformly exhibit positive charges, with the most pronounced positive charges observed proximal to oxygen atoms, which is attributable to the substantial electronegativity of oxygen. Moreover, carbon atoms neighboring oxygen atoms bear positive charges when contrasted with other carbon atoms with a negative charge. The carbon atoms C2 and C7 manifest as the most positively charged within the molecular framework, while the most substantial negative charges reside in C6 and C16.

Fig. 12 (c) and (d) exhibit the electron density distributions for DMTS's HOMO and LUMO, with the energy gap (E_g) of 3.9944 eV signifying its reactivity (Table 9). The HOMO is predominantly localized around the nitrogen and sulfur atoms, indicating these regions as the primary sites for electron donation during adsorption onto the metal surface. In contrast, the LUMO is concentrated around the oxygen atoms and the aromatic ring, suggesting these areas are the main acceptors of electron density. A wide E_g typically indicates stability and low reactivity; however, DMTS's narrower E_g suggests potential as a reactive corrosion inhibitor. The calculated quantum parameters—hardness (η), softness (σ), electronegativity (χ), and electrophilicity index (ω)—reinforce this active behavior. Furthermore, TDOS calculations (Fig. 12 (e)) demonstrate electron density concentration just below the HOMO, predicting electron-donating capabilities conducive to corrosion protection. This denotes DMTS's potential for forming protective surface complexes, affirming its effectiveness as a corrosion inhibitor.

In addition, Fig. 12 (f) and (g) provide a visualization of the electrostatic potential (ESP) mapped onto the electron density surface of the DMTS molecule, offering valuable predictive insight into its site-specific chemical reactivity, particularly for inter-hydrogen bonding and susceptibility to nucleophilic or electrophilic attacks. The ESP plot, derived from DMTS's optimized structure, showcases a range of electrostatic effects: the oxygen atoms are enshrouded by red hues, signaling regions of negative electrostatic potential, typically associated with electrophilic reactivity due to their propensity to attract positive charges, such as protons. Conversely, areas displaying blue—most prominently around hydrogen atoms—indicate positive potential, suggesting nucleophilic reactivity where there is a tendency to repel protons [98–100]. The subtler green areas traversing the π-system denote regions of neutral electrostatic potential. These zones are not typically involved in polar interactions but can engage in hydrophobic interactions, affecting the molecule's orientation and interaction with other non-polar substrates, such as hydrocarbon-based corrosion products or organic coatings on metal surfaces. The nuanced ESP topography captured in the 3D plot and the corresponding contour map in Fig. 12 (g) allows for the correlation of color-coded potential regions with the likelihood of chemical interaction types, thereby supporting the rational design of corrosion inhibitors with tailored reactivity profiles. Literature corroborates that ESP analyses can significantly contribute to our understanding of molecular behavior in complex systems, such as those encountered in corrosion inhibition [101–103]. The ESP mapping on DMTS thus reinforces the molecule's multifaceted inhibitory function, providing a molecular-level explanation for its observed corrosion resistance in practical applications.

The Electron Localization Function (ELF), delineated through advanced computational analyses via the Multiwfn program and visualized in Fig. 12 (h), offers a nuanced depiction of the electron pair probability density within the optimized geometry of DMTS. ELF serves as a robust indicator of the localization of electron pairs, thereby illuminating the presence and characteristics of chemical bonds and molecular structure [104–109]. The three-dimensional (3D) shaded surface maps that project ELF substantiate the hydrogen-bonding propensities of DMTS and articulate the molecule's spatial accommodation on metal substrates. Fig. 12 (h) vividly illustrates the regions of high electron localization, indicative of potential sites for chemical bonding. These sites are integral to the molecule's ability to form stable interactions with metallic surfaces, which is critical to its function as a corrosion inhibitor. The topographical contours of the ELF surface maps emphasize the molecule's geometric suitability for interfacing with the intricate landscapes of metal surfaces. Consequently, the inherent electron distribution within DMTS, as illustrated by the ELF, directly contributes to its efficacy as a corrosion inhibitor, offering a tangible molecular foundation for its protective actions in corrosion-prone environments.

Non-covalent interaction (NCI) analysis provides a meticulous evaluation of the interactions between the DMTS inhibitor and a Fe_{60} cluster, shedding light on the fundamental nature of their interactions, as visualized in Fig. 13. Through the lens of Reduced Density Gradient (RDG) values and color-coded isosurfaces, NCI theory interprets the
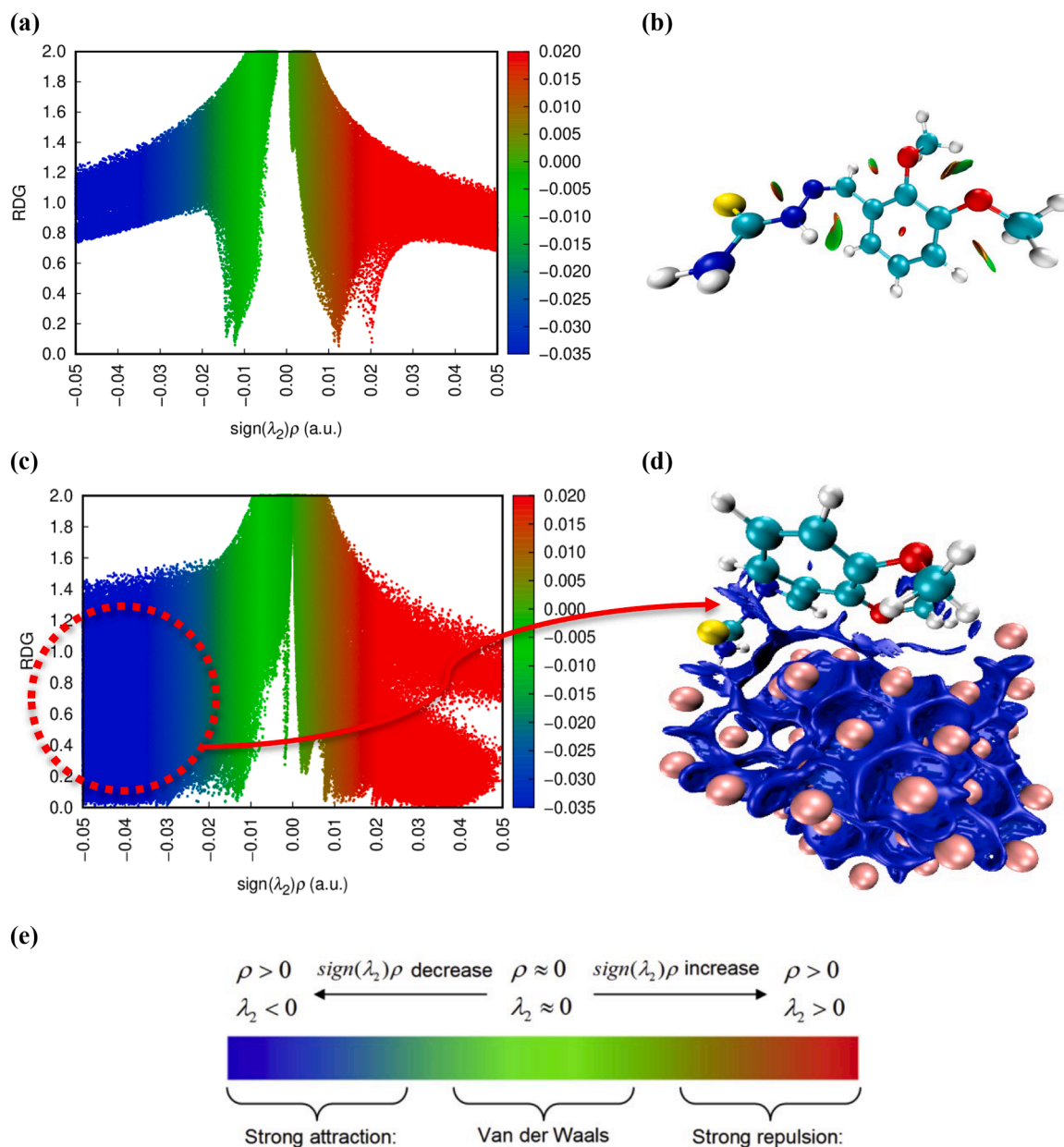
Fig. 13. Non-covalent interaction (NCI) between the DMTS and a Fe$_{60}$ cluster. The RDG scatter plots and NCI plots isosurface (s = 0.5 a.u.) of DMTS inhibitor (a and b), as well as its interacting system with metal (IGM = 0.01 a.u.). The color of the isosurface depends on the sign values (λ_2) ρ, from − 0.05 to 0.05 a.u.

delicate interplay of forces governing the inhibitor-metal surface inter-activity [43,73,81]. The NCI-RDG scatter plots (Fig. 13 (a) and (b)) graphically represent these interactions: blue signifies hydrogen bonding, green indicates van der Waals interactions, and red conveys steric repulsion. The plots articulate a comprehensive spectrum of interaction intensities, with the RDG isovalue extending from −0.035 to 0.020 a.u., investigative regions of stability and potential reactivity on the metal surface. The red regions in the scatter plot allude to mitigated steric repulsion resulting from DMTS's molecular architecture, which is rich in electron-donating heteroatoms.

Conversely, blue and green areas reflect the inhibitor's effective non-covalent bonding, which is fundamental in forming a protective layer on steel surfaces in corrosive environments. RDG versus sign (λ_2) × ρ plots (Fig. 13 (c) and (d)) further differentiate the bonding landscape, marking the strength and nature of interactions at the inhibitor-metal interface. The prominence of green zones in these plots signifies the substantial role of van der Waals forces, indicative of the influence of

DMTS's molecular structure on the inhibition mechanism.

The NCI analysis aligns with previous discussions on the results of FMO, Mulliken charge, MEP, and ELF investigations, shedding light on the bonding and reactivity properties of the DMTS molecule and providing a holistic view of DMTS's protective efficacy against corrosion on metallic substrates. Integrating NCI studies with computational and experimental data corroborates the inhibitor's effectiveness, portraying how DMTS molecular interactions contribute to forming a resilient adsorptive layer on metal surfaces. Consequently, this comprehensive understanding enriches our knowledge of corrosion inhibition and supports the utilization of DMTS as a formidable defense against metal degradation.

3.10.2. Monte Carlo simulations

Fig. 14 illustrates the molecular adsorption of the inhibitor DMTS and its protonated form, PDMTS, onto an iron (110) surface. The sim-ulations reveal that both inhibitors orient almost flatly on the surface,
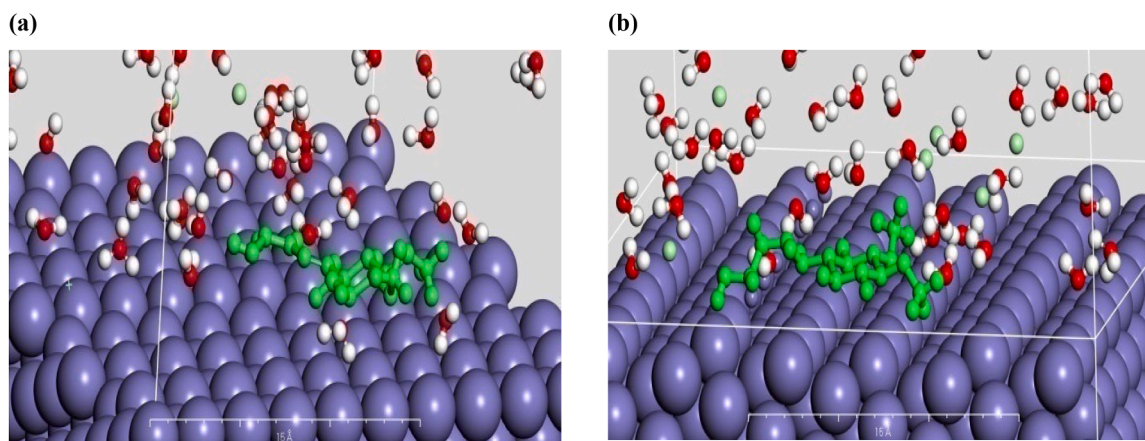
(a) **(b)**

Fig. 14. Neutral DMTS (a) and protonated DMTS (b) adsorption on the steel surface.

Table 10
MCS outputs for the Fe(100)/Inhibitor (1)/water (50)/HCl (10) System's lowest adsorption configuration. Energies are in kcal/mol.

Aqueous solution						
	Total energy	Adsorption energy	Rigid adsorption energy	Deformation energy	dEad/dNi	
					H_2O	Mol
DMTS	−7.88	−1425.30	−29.00	−1396.30	−10.13	−193.11
Protonated DMTS	−5.51	−1441.75	−32.10	−1409.65	−10.87	−206.81

Acidic aqueous solution							
	Total energy	Adsorption energy	Rigid adsorption energy	Deformation energy	dEad/dNi		
					H_2O	Mol	Cl^-	H_3O^+
DMTS	−13.55	−1728.24	−40.81	−1687.43	−10.23	−186.18	−0.27	−28.47
PDMTS	−16.73	−1750.25	−44.64	−1705.61	−9.92	−208.00	−28.12	−1.42

Consequently, MC simulations confirm that DMTS and PDMTS are highly effective in adsorbing onto the iron (110) surface. Their strong interactions with the surface, as evidenced by favorable thermodynamic and stability parameters, contribute significantly to their efficacy as corrosion inhibitors in both aqueous and acidic environments. While these computational findings provide valuable theoretical insights, it is crucial to validate them against experimental evidence to ensure their practical applicability. This validation will enhance the robustness of the conclusions drawn from the simulations. Nevertheless, the demonstrated efficacy of DMTS and PDMTS underscores their potential as superior inhibitors for corrosion protection applications in industrial settings where XC38 steel is utilized.

which is optimal for achieving maximum adsorptive interaction with the metal substrate. Table 10 presents detailed thermodynamic parameters from MC simulations in both aqueous and HCl solutions. The parameters include total energy, adsorption energy, rigid adsorption energy, deformation energy, and dEad/dNi—a critical descriptor that evaluates the stability of the adsorption system on a molecular level. These simulations show that DMTS and PDMTS exhibit negative adsorption energies in neutral and acidic environments, indicating exothermic and spontaneous adsorption processes [27,65,110,111]. This spontaneous nature of adsorption underscores a robust interaction between the inhibitors and the iron surface, suggesting a strong capability for adsorption and corrosion inhibition. The analysis of dEad/dNi values is particularly significant. A higher absolute value in this descriptor implies a stronger and more stable inhibitor-Fe interaction, pivotal for enhancing corrosion inhibition efficiency. These findings suggest that in the presence of water and chloride ions, both DMTS and PDMTS are more effective in displacing these species from the iron surface, thereby protecting the metal more efficiently [112].
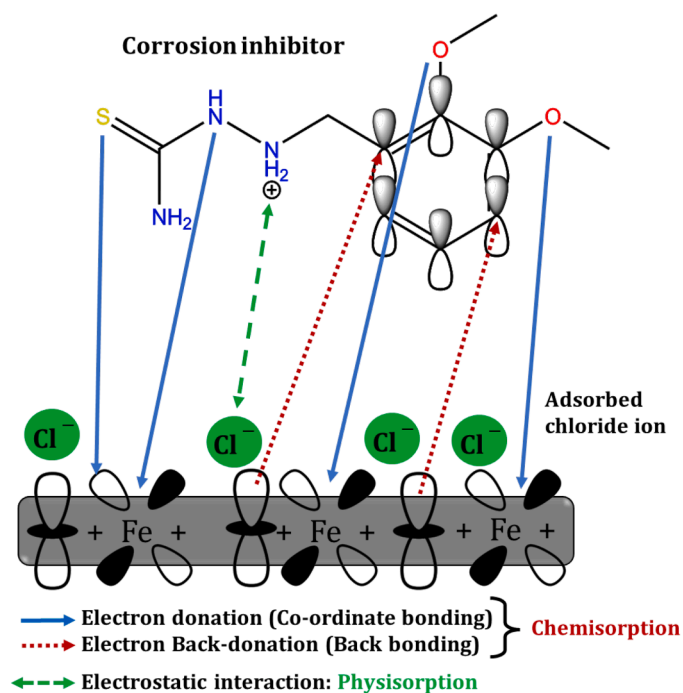
3.11. Inhibition mechanism

Understanding the detailed processes that prevent corrosion at the interface between XC38 carbon steel and hydrochloric acid solutions is crucial for developing effective corrosion inhibitors. Scheme 4 illustrates the complex interactions involved in this system, combining theoretical insights and experimental validations. The interaction commences in the acidic environment of HCl, leading to the active sites' protonation on the

DMTS inhibitor. Computational analyses suggest that protonation predominantly occurs at the sulfur atom, followed by the nitrogen atom. In the corrosive conditions typical of 1 M HCl, the metal surface quickly oxidizes and becomes positively charged. This oxidation attracts negatively charged chloride ions from the HCl, resulting in a negatively charged metal surface. The altered charge on the metal surface enhances the physical adsorption of the protonated inhibitors due to electrostatic forces, promoting a swift initial adsorption phase [90,113]. The presence of conjugated double bonds and the electron-rich lone pairs on the nitrogen, sulfur, and oxygen atoms facilitate further adsorption through donor-acceptor interactions [36,114].

These interactions initiate chemisorption, which involves the transfer of electrons from the inhibitor's active sites to the steel's unoccupied d orbitals (electron donation). This is followed by a return flow of electrons from the steel's d orbitals to the electron-deficient areas of the inhibitor (back-donation), as depicted in Scheme 4. This exchange strengthens the bond between the inhibitor and the metal surface, providing a robust protective layer against further corrosion. In this sequence, water molecules initially adsorbed on the metal surface are displaced by DMPTS molecules, characterized by their polar groups and heteroatoms, further facilitating the adsorption process [74,115,116].

This displacement is crucial as it clears the way for the inhibitor to form a direct bond with the metal surface, increasing the effectiveness of the corrosion protection. Both experimental and theoretical research affirm that chemisorption is the dominant mechanism in this adsorption process, though a minor component of physisorption remains possible [117–120]. Upon careful evaluation, it is apparent that the adsorption of

Scheme 4. Schematic illustration of the adsorption mechanism of DMTS inhibitor on XC38 carbon steel surface in 1 M HCl solution.

DMPTS on XC38 in 1M HCl predominantly involves intertwined mechanisms of physisorption and chemisorption through electron donation and back-donation [113,121]. Thus, this comprehensive exploration provides essential insights into the intricate sequence of events leading to the adsorption of inhibitors on the metal surface, thus enhancing our understanding of corrosion inhibition. The detailed analysis merges theoretical predictions with experimental observations to confirm the effectiveness of DMPTS as a corrosion inhibitor in acidic environments.

3.12. Comparative analysis with literature data

The efficacy of DMTS as a corrosion inhibitor for XC38 carbon steel in a 1 M HCl solution stands out remarkably when benchmarked against traditional and novel corrosion inhibitors. This comparative analysis draws upon empirical data and theoretical insights to underscore the superior performance and potential groundbreaking advancements DMTS introduces in corrosion inhibition. Table 11 offers a comprehensive overview of the inhibition efficiencies of various inhibitors under similar experimental conditions. The inhibitors compared include a variety of aromatic and aliphatic compounds tested primarily on mild and carbon steel substrates in 1 M HCl medium. DMTS, at a concentration of just 100 ppm, demonstrates an exceptional inhibition efficiency, reflected in a 98.14 % reduction in weight loss, 94.00 % efficiency in PDP tests, and 93.53 % effectiveness in EIS analysis. These results are particularly noteworthy considering the low concentration used, highlighting the high activity and potency of DMTS. The inhibitors listed in Table 11, such as 2-PCT, 3-PCT, 4-PCT, and others, typically operate through a mixed mechanism involving physical and chemical adsorption. Their reported efficiencies vary, with the highest efficiencies often seen at considerably higher concentrations (1.5 mM or 10 mM) than DMTS. For example, 1A, 1B, and 1C demonstrate efficiencies ranging from 88.00 % to 97.00 % in PDP tests at a concentration of 10 mM [122]. In contrast, DMTS achieves similar or superior efficiency at a significantly lower concentration. The statistical analysis further substantiates the high efficiency of DMTS. DMTS exhibits a consistent performance across different experimental methods compared to traditional inhibitors, affirming its robustness and reliability as a corrosion

inhibitor. Theoretical studies suggest that the high efficiency of DMTS could be attributed to its molecular structure, which facilitates both strong adsorption capabilities and the effective formation of protective layers on the metal surface. The innovation brought by DMTS extends beyond its high corrosion inhibition efficiency. Theoretical insights reveal that its molecular structure allows for optimized interaction with the metal surface, involving complex bonding mechanisms that enhance both the initiation and stability of the adsorption process. This multifaceted interaction reduces the corrosion rate and enhances the inhibitor's resistance to environmental factors within the corrosive medium. Accordingly, DMTS represents a significant advancement in corrosion inhibition technology for XC38 carbon steel in acidic environments. Its ability to achieve high inhibition efficiency at low concentrations and robust performance across various testing protocols position it as a groundbreaking solution in the ongoing battle against metal corrosion. The comparative analysis with literature data confirms the superior performance of DMTS and highlights its potential as a more efficient and economical choice in industrial applications (Fig. 2).

4. Conclusion

This study has systematically investigated the corrosion inhibition properties of 3,4-dimethoxy phenyl thiosemicarbazone (DMTS) on XC38 carbon steel in a 1 M hydrochloric acid environment. By blending sophisticated experimental techniques and advanced computational analyses, we have elucidated how DMTS interacts with the steel substrate to provide significant protective effects against corrosion.
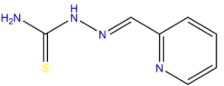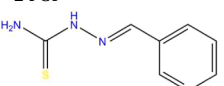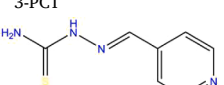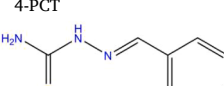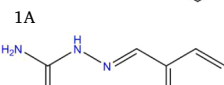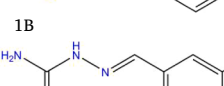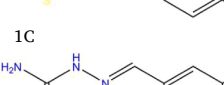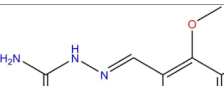
Potentiodynamic polarization measurements demonstrated that DMTS substantially reduces the corrosion rate, with inhibition efficiency reaching up to 94 % at a concentration of 100 ppm. Gravimetric analysis further revealed an inhibition efficiency of 98.14 % at the same concentration. Electrochemical impedance spectroscopy (EIS) results showed an inhibition efficiency of 93.53 %, underscoring the high effectiveness of DMTS in this environment. The observed shift in corrosion potential and decrease in current density indicate the formation of a robust protective layer on the metal surface. Activation thermodynamics and adsorption isotherm studies showed negative ΔG°_{ads} values, indicating spontaneous adsorption. Specifically, a ΔG°_{ads} of -7.812 kJ·mol^{-1} signified a physisorptive interaction, characterized by electrostatic forces rather than charge sharing. Surface analyses using SEM, EDS, AFM, and XRD confirmed the formation of a protective layer on the steel surface. SEM and AFM images revealed a smoother surface morphology in the presence of DMTS, indicating reduced corrosion. EDS results showed a decrease in iron content and an increase in elements associated with the inhibitor, confirming surface adsorption. XRD patterns revealed the absence of iron oxides in the presence of the inhibitor, underscoring its protective effect.

Complementing the experimental data, our computational studies using density functional theory (DFT), Reduced Density Gradient (RDG) analysis, and Monte Carlo simulations provided deep insights into the atomic-level interactions between DMTS and steel. These analyses confirmed that non-covalent interactions, particularly hydrogen bonds and van der Waals forces, play critical roles in the adsorption of DMTS onto the steel surface, facilitating a stable and durable barrier against corrosion.

The integration of experimental and computational findings in this study enhances our understanding of Schiff base compounds as effective corrosion inhibitors and positions DMTS as a particularly potent inhibitor in acidic conditions. The detailed analysis of non-covalent interactions further enriches the theoretical framework for corrosion inhibition, offering pathways for developing new inhibitors based on Schiff base chemistry.

The findings from this study underscore the significant potential for using DMTS and other Schiff base compounds in industries where corrosion protection is critical. Given the pressing need for effective

Table 11

Comparative analysis of corrosion inhibition efficiency of DMTS in comparison to selected literature findings.

Inhibitor	Testing conditions	Inhibitor concentration	Efficiency (%)	Type of inhibitor & Adsorption	Ref.
2-PCT	Mild steel, 1 M HCl	1.5 mM	PDP: 88.80 EIS: 92.00	Mixed-type with both physical and chemical adsorption	[123]
3-PCT	Mild steel, 1 M HCl	1.5 mM	WL: 97.00 PDP: 88.00 EIS: 92.00	Mixed-type with physisorption mechanism	[124]
4-PCT	Mild steel, 1 M HCl	1.5 mM	PDP: 84.80 EIS: 85.50	Mixed-type with both physical and chemical adsorption	[123]
1A	AISI 1020 carbon steel, 1 M HCl	10 mM	PDP: 97.00 EIS: 93.00	Mixed-type with both physical and chemical adsorption	[122]
1B	AISI 1020 carbon steel, 1 M HCl	10 mM	PDP: 88.00 EIS: 90.00	Mixed-type with both physical and chemical adsorption	[122]
1C	AISI 1020 carbon steel, 1 M HCl	10 mM	PDP: 97.00 EIS: 93.00	Mixed-type with both physical and chemical adsorption	[122]
TMBHC	Mild steel, 1 M HCl	0.8 mM	PDP: 89.80 EIS: 87.90	Mixed-type with chemical adsorption	[125]
DMTS	**XC38 carbon steel, 1 M HCl**	**100 ppm**	**WL: 98.14 PDP: 94.00 EIS: 93.53**	**Mixed-type with physisorption mechanism**	**This work**

corrosion management in industrial settings, these results are highly impactful. They suggest that Schiff bases, with their incorporation of heteroatoms like nitrogen, sulfur, and oxygen, can be developed into cost-effective, efficient, and environmentally friendly solutions for corrosion control. These compounds form stable and protective adsorption layers on metal surfaces, thereby impeding corrosion processes.

Future research should investigate the scalability of producing Schiff base inhibitors at an industrial level, ensuring economic feasibility. Assessing the long-term stability of these inhibitors under various operational conditions is crucial to guarantee sustained corrosion protection over time. Moreover, evaluating the environmental impact of using Schiff base inhibitors, including their biodegradability and potential ecological effects, is essential for their sustainable use. Studies should also focus on synthesizing new Schiff base compounds and optimizing their concentrations for maximum efficiency in industrial applications, particularly under different corrosive conditions encountered in various sectors. Ensuring that the use of these inhibitors aligns with environmental regulations and sustainability goals will make them suitable for widespread industrial adoption.

The study was conducted under controlled laboratory conditions using specific concentrations of DMTS and a 1 M HCl solution. However, real-world applications may present additional challenges, such as varying environmental conditions, the presence of other chemicals, and mechanical stresses that could influence the inhibitor's performance. Moreover, the study did not fully explore the long-term stability of DMTS under continuous exposure to corrosive environments. Future research should investigate the durability of the inhibitor over extended periods to ensure sustained protection. The potential environmental effects of DMTS, including its biodegradability and ecological impact, were also not addressed in this study. Understanding these factors is crucial for the sustainable use of Schiff base inhibitors in industrial applications. While computational studies provided valuable theoretical insights into the molecular interactions between DMTS and the steel surface, these simulations are based on idealized models that may not fully capture the complexity of real-world systems. Therefore, additional experimental validation is necessary to confirm these findings. Future research should aim to more thoroughly compare computational predictions with experimental evidence to enhance the validity and applicability of the theoretical models used in this study.

In conclusion, this study not only contributes to the field of corrosion science by providing a detailed mechanistic understanding of how DMTS inhibits steel corrosion but also opens avenues for further research into corrosion inhibitors that are both effective and sustainable. Through continued interdisciplinary research, developing novel corrosion inhibitors that align with industry needs and environmental standards can

be significantly advanced.

CRediT authorship contribution statement

Smail Brioua: Writing – original draft, Visualization, Validation, Investigation, Formal analysis, Data curation, Conceptualization. **Amel Delimi:** Writing – original draft, Visualization, Investigation, Formal analysis, Conceptualization. **Hana Ferkous:** Writing – original draft, Supervision, Investigation, Formal analysis, Conceptualization. **Said Boukerche:** Investigation, Formal analysis, Conceptualization. **Hamza Allal:** Visualization, Investigation, Formal analysis, Conceptualization. **Abir Boublia:** Writing – review & editing, Writing – original draft, Visualization, Validation, Investigation, Formal analysis, Conceptualization. **Amel Djedouani:** Investigation. **Malika Berredjem:** Resources, Investigation. **Abdesalem Kahlouche:** Investigation, Formal analysis. **Khadidja Otmane Rachedi:** Writing – original draft, Validation, Investigation. **Amdjed Abdennouri:** Investigation, Formal analysis, Conceptualization. **Manawwer Alam:** Writing – review & editing. **Barbara Ernst:** Writing – review & editing. **Yacine Benguerba:** Writing – review & editing, Visualization, Supervision, Formal analysis, Conceptualization.

Declaration of interests

The authors declare that they have no known competing financial interests or personal relationships that could have appeared to influence the work reported in this paper.

References

[1] Ferkous H, Sedik A, Delimi A, Redjemia R, Abdesalem K, Boulechfar C, et al. A comparative study of novel synthesized sulfamide compounds: electrochemical, morphological, XPS, and theoretical investigations on copper corrosion inhibition in 1.0 M HCl. J Mol Liq 2024;394:123781. https://doi.org/10.1016/j. molliq.2023.123781.

[2] Zaher A, Aslam R, Lee HS, Khafouri A, Boufellous M, Alrashdi AA, et al. A combined computational & electrochemical exploration of the Ammi visnaga L. extract as a green corrosion inhibitor for carbon steel in HCl solution. Arab J Chem 2022;15:103573. https://doi.org/10.1016/j.arabjc.2021.103573.

[3] Gabsi M, Ferkous H, Delimi A, Boublia A, Boulechfar C, Kahlouche A, et al. The curious case of polyphenols as green corrosion inhibitors: a review on their extraction, design, and applications. Environ Sci Pollut Res 2023;30:59081–105. https://doi.org/10.1007/s11356-023-26753-4.

[4] Arrousse N, Fernine Y, Haldhar R, Berdimurodov E, Ichou H, Al-Zaqri N, et al. Corrosion protection studies of different alloys in 1 M HCl by benzimidazole derivative: combined molecular dynamic simulations/DFT. J Environ Chem Eng 2023;11:109642. https://doi.org/10.1016/j.jece.2023.109642.

[5] Umoren SA, Suleiman RK, Obot IB, Solomon MM, Adesina AY. Elucidation of corrosion inhibition property of compounds isolated from Butanolic Date Palm Leaves extract for low carbon steel in 15 % HCl solution: experimental and theoretical approaches. J Mol Liq 2022;356:119002. https://doi.org/10.1016/j. molliq.2022.119002.

[6] Papadaki M, Demadis KD. Structural mapping of hybrid metal phosphonate corrosion inhibiting thin films. Comments Inorg Chem 2009;30:89–118. https://doi.org/10.1080/02603590903320916.

[7] Zakeri A, Bahmani E, Aghdam ASR. Plant extracts as sustainable and green corrosion inhibitors for protection of ferrous metals in corrosive media: a mini review. Corros Commun 2022;5:25–38. https://doi.org/10.1016/j. corcom.2022.03.002.

[8] Boublia A, Guezzout Z, Haddaoui N, Badawi M, Darwish AS, Lemaoui T, et al. Enhancing precision in PANI/Gr nanocomposite design: robust machine learning models, outlier resilience, and molecular input insights for superior electrical conductivity and gas sensing performance. J Mater Chem A 2023;12:2209–36. https://doi.org/10.1039/d3ta06385b.

[9] Boublia A, Guezzout Z, Haddaoui N, Badawi M, Darwish AS, Lemaoui T, et al. The curious case of polyaniline-graphene nanocomposites: a review on their application as exceptionally conductive and gas sensitive materials. Crit Rev Solid State Mater Sci 2023;0:1–25. https://doi.org/10.1080/10408436.2023.2274900.

[10] Al Jahdaly BA, Maghraby YR, Ibrahim AH, Shouier KR, Alturki AM, El-Shabasy RM. Role of green chemistry in sustainable corrosion inhibition: a review on recent developments. Mater Today Sustain 2022;20:100242. https://doi.org/10.1016/j.mtsust.2022.100242.

[11] Belakhdar A, Ferkous H, Djellali S, Lahbib H, Ben AY. Thermodynamic and electrochemical studies of corrosion inhibition of carbon steel by rosmarinus officinalis extract in acid medium. Environ. Sci. Eng. Springer; 2021. p. 1479–83. https://doi.org/10.1007/978-3-030-51210-1_236.

[12] Du P, Yang H, Deng S, Li X. Synergistic inhibition of Mikania micrantha extract with iodide ion on the corrosion of cold rolled steel in trichloroacetic acid medium. J Ind Eng Chem 2024;220:111296. https://doi.org/10.1016/j. jiec.2024.05.014.

[13] Boulechfar C, Ferkous H, Djellali S, Amin MA, Boufas S, Djedouani A, et al. DFT/molecular scale, MD simulation and assessment of the eco-friendly anti-corrosion performance of a novel Schiff base on XC38 carbon steel in acidic medium. J Mol Liq 2021;344:117874. https://doi.org/10.1016/j.molliq.2021.117874.

[14] Meriem Z, Hana F, Souad D, Abderrazak B, Amin MA, Leila R, et al. Experimental and theoretical evaluation of the adsorption process of some polyphenols and their corrosion inhibitory properties on mild steel in acidic media. J Environ Chem Eng 2021;9:106482. https://doi.org/10.1016/j.jece.2021.106482.

[15] Shanmugapriya R, Ravi M, Ravi S, Ramasamy M, Maruthapillai A, AS J. Electrochemical and morphological investigations of elettaria cardamomum pod extract as a green corrosion inhibitor for Mild steel corrosion in 1 N HCl. Inorg Chem Commun 2023;154:110958. https://doi.org/10.1016/j. inoche.2023.110958.

[16] Ferkous H, Djellali S, Sahraoui R, Benguerba Y, Behloul H, Çukurovali A. Corrosion inhibition of mild steel by 2-(2-methoxybenzylidene) hydrazine-1-carbothioamide in hydrochloric acid solution: experimental measurements and quantum chemical calculations. J Mol Liq 2020;307:112957. https://doi.org/10.1016/j.molliq.2020.112957.

[17] Boulechfar C, Ferkous H, Delimi A, Djedouani A, Kahlouche A, Boublia A, et al. Schiff bases and their metal complexes: a review on the history, synthesis, and applications. Inorg Chem Commun 2023;150:110451. https://doi.org/10.1016/j. inoche.2023.110451.

[18] Aroui L, Madani S, Bousnoubra I, Boublia A, Lakikza I, Imene Aouni S, Abdelouahed L, Ernst B, Alam M, Benguerba Y. Enhanced degradation of crystal violet using PANI-ZnO nanocomposites: Electro-oxidation and photocatalysis studies. J. Mol. Liq. 2024:125818. https://doi.org/10.1016/j. molliq.2024.125818.

[19] Ferkous H, Djellali S, Sahraoui R, Behloul H, Saoud K, Çukurovali A. Electrochemical impedance spectroscopy and adsorption study of carbon steel in 1 M HCl solution containing 2-(2-methoxybenzylidene) hydrazine-1-carbothioamide. Springer International Publishing; 2021. https://doi.org/10.1007/978-3-030-51210-1_9.

[20] El-Azabawy OE, Higazy SA, Al-Sabagh AM, Abdel-Rahman AAH, Nasser NM, Khamis EA. Studying the temperature influence on carbon steel in sour petroleum media using facilely-designed Schiff base polymers as corrosion inhibitors. J Mol Struct 2023;1275:134518. https://doi.org/10.1016/j.molstruc.2022.134518.

[21] Gupta SK, Mitra RK, Yadav M, Dagdag O, Berisha A, Mamba BB, et al. Electrochemical, surface morphological and computational evaluation on carbohydrazide Schiff bases as corrosion inhibitor for mild steel in acidic medium. Sci Rep 2023;13:15108. https://doi.org/10.1038/s41598-023-41975-9.

[22] Bouchareb F, Berredjem M, Dehmchi DA, Kadri R, Kadri M, Ferkous H, et al. Synthesis, characterization, DFT/M06 studies, NBO, QTAIM and RDG analyses of new copper (II) complexes with bis-phosphonamide obtained under microwave irradiation. J Mol Struct 2023;1294:136503. https://doi.org/10.1016/j. molstruc.2023.136503.

[23] Wang J, An L, Wang J, Gu J, Sun J, Wang X. Frontiers and advances in N-heterocycle compounds as corrosion inhibitors in acid medium: recent advances. Adv Colloid Interface Sci 2023;321:103031. https://doi.org/10.1016/j. cis.2023.103031.

[24] Zhang W, Wang S, Guo Z, Luo J, Zhang C, Zhang G. Heterocyclic group end-capped polyethylene glycol: synthesis and used as corrosion inhibitors for mild steel in HCl medium. J Mol Liq 2023;388:122779. https://doi.org/10.1016/j. molliq.2023.122779.

[25] Benzouid H, Boudebane S, Ferkous H, Lekoui F, Bin NN, Delimi A, et al. Examining the microstructure, morphological features, and wetting characteristics of Ti/TiN/TiAlN thin films produced through RF/DC magnetron co-sputtering. Mater Today Commun 2023;37:107405. https://doi.org/10.1016/j.mtcomm.2023.107405.

[26] Kaya F, Solmaz R, Geçibesler İH. Adsorption and corrosion inhibition capability of Rheum ribes root extract (Işgın) for mild steel protection in acidic medium: a comprehensive electrochemical, surface characterization, synergistic inhibition effect, and stability study. J Mol Liq 2023;372:121219. https://doi.org/10.1016/j.molliq.2023.121219.

[27] Yasmin T, Mahmood A, Farooq M, Rehman U, Sarfraz RM, Ijaz H, et al. Quince seed mucilage/β-cyclodextrin/Mmt-Na+-co-poly (methacrylate) based pH-sensitive polymeric carriers for controlled delivery of Capecitabine. Int J Biol Macromol 2023;253:127032. https://doi.org/10.1016/j.ijbiomac.2023.127032.

[28] Mahmood A, Mahmood A, Sarfraz RM, Hussain Z, Afzal A, Boublia A, et al. Chitosan-based intelligent polymeric networks for site-specific colon medication delivery: a comprehensive study on controlled release of diloxanide furoate and network formation dynamics. Int J Biol Macromol 2024;255:128089. https://doi.org/10.1016/j.ijbiomac.2023.128089.

[29] Belakhdar A, Ferkous H, Djellali S, Sahraoui R, Lahbib H, Ben Amor Y. Corrosion inhibition performance of rosmarinus officinalis methanolic corrosion inhibition performance of rosmarinus officinalis methanolic extract on carbon steel XC48 in acidic medium (2M HCl). Mater Biomater Sci 2020;03:46–53.

[30] Boulechfar C, Ferkous H, Boufas S, Berredjem M, Delimi A, Djellali S, et al. Synthesis, electrochemical, and quantum chemical studies of some metal complexes: Mn(II), Co(II), and Zn(II) with 2-furaldehyde semicarbazone. J Mol Struct 2023;1271:134007. https://doi.org/10.1016/j.molstruc.2022.134007.

[31] Ferkous H, Zerroug M, Radjai M, Chaouch MA, Jebali Z, Majdoub H. Electrochemical and surface morphological studies of a carbon steel corrosion by natural product in acidic solution. Adv Sci Technol Innov 2018:1291–2. https://doi.org/10.1007/978-3-319-70548-4_379. Springer.

[32] Xu Z, Cao X, Wang Y, Slaný M, Unčík S, Li S, et al. Effective corrosion inhibitor of mild steel in marine environments: synthesis and application of hydrazides. Sustain Mater Technol 2023;38:e00747. https://doi.org/10.1016/j.susmat.2023.e00747.

[33] Mouats N, Djellali S, Ferkous H, Sedik A, Delimi A, Boublia A, et al. Comprehensive investigation of the adsorption, corrosion inhibitory properties, and quantum calculations for 2-(2,4,5-trimethoxybenzylidene) hydrazine carbothioamide in mitigating corrosion of XC38 carbon steel under HCl environment. ACS Omega 2024. https://doi.org/10.1021/acsomega.3c10240.

[34] Wamba-Tchio OR, Pengou M, Teillout AL, Baumier C, Mbomekallé IM, De Oliveira P, et al. Electrochemical study and experimental simulation of the synergistic effect of a formulation based on Ficus pumila Linn. Leaves extract and zinc sulfate on the XC38 steel corrosion inhibition in NaCl solution. J Electroanal Chem 2022;919:116553. https://doi.org/10.1016/j.jelechem.2022.116553.

[35] Ichchou I, Larabi L, Rouabhi H, Harek Y, Fellah A. Electrochemical evaluation and DFT calculations of aromatic sulfonohydrazides as corrosion inhibitors for XC38 carbon steel in acidic media. J Mol Struct 2019;1198:126898. https://doi.org/10.1016/j.molstruc.2019.126898.

[36] Boukerche S, Ferkous H, Delimi A, Sedik A, Djedouani A, Otmane Rachedi K, et al. Anti-corrosion performance of dehydroacetic acid thiosemicarbazone on XC38 carbon steel in an acidic medium. Arab J Chem 2023;16:105061. https://doi.org/10.1016/j.arabjc.2023.105061.

[37] Bilgiç S. Plant extracts as corrosion inhibitors for mild steel in HCl media - review I. Int J Corros Scale Inhib 2021;10:145–75. https://doi.org/10.17675/2305-6894-2021-10-1-9.

[38] Aljibori HS, Abdulzahra OH, Al Adily AJ, Al-Azzawi WK, Al-Amiery AA, Kadhum AAH. Recent progresses in thiadiazole derivatives as corrosion inhibitors in hydrochloric acid solution. Int J Corros Scale Inhib 2023;12:842–66. https://doi.org/10.17675/2305-6894-2023-12-3-3.

[39] Gupta SK, Mehta RK, Yadav M, Dagdag O, Mehmeti V, Berisha A, et al. Diazenyl derivatives as efficient corrosion inhibitors for mild steel in HCl medium: gravimetric, electrochemical and computational approach. J Mol Liq 2023;382:121976. https://doi.org/10.1016/j.molliq.2023.121976.

[40] Elqars E, Laamari Y, Sadik K, Bimoussa A, Oubella A, Mechnou I, et al. Synthesis, experimental, theoretical, and molecular studies of 1-(2,5-dimethoxy-4-methylphenyl)ethan-1-thiosemicarbazone as green inhibitor for carbon steel corrosion. J Mol Struct 2023;1282:135228. https://doi.org/10.1016/j.molstruc.2023.135228.

[41] Delimi A, Ferkous H, Alam M, Djellali S, Sedik A, Abdesalem K, et al. Corrosion protection performance of silicon-based coatings on carbon steel in NaCl solution: a theoretical and experimental assessment of the effect of plasma-enhanced chemical vapor deposition pretreatment. RSC Adv 2022;12:15601–12. https://doi.org/10.1039/d1ra08848c.

[42] Lemaoui T, Boublia A, Lemaoui S, Darwish AS, Ernst B, Alam M, Benguerba Y, Banat F, AlNashef IM. Predicting the CO2 Capture Capability of Deep Eutectic Solvents and Screening over 1000 of their Combinations Using Machine Learning. ACS Sustain. Chem. Eng. 2023;11:9564–80. https://doi.org/10.1021/acssuschemeng.3c00415.

[43] Benachour N, Delimi A, Allal H, Boublia A, Sedik A, Ferkous H, et al. 3,4-Dimethoxy phenyl thiosemicarbazone as an effective corrosion inhibitor of copper under acidic solution: comprehensive experimental, characterization and theoretical investigations. RSC Adv 2024;14:12533–55. https://doi.org/10.1039/d3ra08629a.

[44] Ramdane N, Marsa Z, Delimi A, Sedik A, Boublia A, Albakri GS, et al. Synergistic shielding of copper from nitric acid corrosion: unveiling the mechanisms through electrochemical, characterization, and computational insights with 2-Hydroxy-benzaldehyde oxime. Inorg Chem Commun 2024;165:112479. https://doi.org/10.1016/j.inoche.2024.112479.

[45] Frisch A. Gaussian 09W Reference. others. 2009. p. 470. Wallingford, USA25p.

[46] Dennington RII, Keith T, Millam J, Eppinnett K, Hovell WL, Gilliland R. GaussView v. 5.0. 9 visualizer and builder. Wallingford, CT: Gaussian Inc; 2009.

[47] Moumeni O, Mehri M, Kerkour R, Boublia A, Mihoub F, Rebai K, et al. Experimental and detailed DFT/MD simulation of α-aminophosphonates as promising corrosion inhibitor for XC48 carbon steel in HCl environment.

[48] Islam Touahria Y, Chafai N, Moumeni O, Boublia A, Mehri M, Benguerba Y. Synthesis, characterization, and comprehensive computational analysis of aromatic hydrazone compounds: unveiling quantum parameters, evaluating antioxidant activity, and investigating molecular docking interactions. J Mol Liq 2024;403:124897. https://doi.org/10.1016/j.molliq.2024.124897.

[49] Elboughdiri N, Ferkous H, Rouibah K, Boublia A, Delima I, Yadav KK, et al. Comprehensive investigation of Cu2+ adsorption from wastewater using olive-waste-derived adsorbents: experimental and molecular insights. Int J Mol Sci 2024;25. https://doi.org/10.3390/ijms25021028.

[50] Elboughdiri N, Lakikza I, Boublia A, Aouni SI, El Houda Hammoudi N, Georgin J, et al. Application of statistical physical, DFT computation and molecular dynamics simulation for enhanced removal of crystal violet and basic fuchsin dyes utilizing biosorbent derived from residual watermelon seeds (Citrullus lanatus). Process Saf Environ Prot 2024;186:995–1010. https://doi.org/10.1016/j.psep.2024.03.093.

[51] AlYammahi J, Darwish AS, Lemaoui T, Boublia A, Benguerba Y, AlNashef IM, et al. Molecular guide for selecting green deep eutectic solvents with high monosaccharide solubility for food applications. ACS Omega 2023;8:26533–47. https://doi.org/10.1021/acsomega.3c03326.

[52] Boublia A, Lemaoui T, AlYammahi J, Darwish AS, Ahmad A, Alam M, et al. Multitask neural network for mapping the glass transition and melting temperature space of homo- and co-polyhydroxyalkanoates using σ profiles molecular inputs. ACS Sustain Chem Eng 2023;11:208–27. https://doi.org/10.1021/acssuschemeng.2c05225.

[53] Himeur T, Rouibah K, Ferkous H, Boublia A, Rachedi KO, Harouche K, et al. Unlocking the power of inula viscosa essential oil: a green solution for corrosion inhibition in XC48 steel within acidic environments. Process Saf Environ Prot 2024. https://doi.org/10.1016/j.psep.2024.05.061.

[54] Kaabi I, Amamra S, Douadi T, Al-Noaimi M, Chafai N, Boublia A, et al. Unveiling the dual role of a novel azomethine: corrosion inhibition and antioxidant potency – a multifaceted study integrating experimental and theoretical approaches. J Taiwan Inst Chem Eng 2024;161:105535. https://doi.org/10.1016/j.jtice.2024.105535.

[55] Uka D, Blagojević B, Alioui O, Boublia A, Elboughdiri N, Benguerba Y, et al. An innovative and environmentally friendly approach for resveratrol solubilization and bioaccessibility enhancement by using natural deep eutectic solvents. J Mol Liq 2023;391:123411. https://doi.org/10.1016/j.molliq.2023.123411.

[56] Lemaoui T, Darwish AS, Almustafa G, Boublia A, Sarika PR, Jabbar NA, et al. Machine learning approach to map the thermal conductivity of over 2,000 neoteric solvents for green energy storage applications. Energy Storage Mater 2023;59:102795. https://doi.org/10.1016/j.ensm.2023.102795.

[57] Boublia A, Lemaoui T, Abu Hatab F, Darwish AS, Banat F, Benguerba Y, et al. Molecular-based artificial neural network for predicting the electrical conductivity of deep eutectic solvents. J Mol Liq 2022;366:120225. https://doi.org/10.1016/j.molliq.2022.120225.

[58] Lemaoui T, Boublia A, Darwish AS, Alam M, Park S, Jeon BH, et al. Predicting the surface tension of deep eutectic solvents using artificial neural networks. ACS Omega 2022;7:32194–207. https://doi.org/10.1021/acsomega.2c03458.

[59] Mouffok A, Bellouche D, Debbous I, Anane A, Khoualdia Y, Boublia A, et al. Synergy of garlic extract and deep eutectic solvents as promising natural antibiotics: experimental and COSMO-RS. J Mol Liq 2023;375:121321. https://doi.org/10.1016/j.molliq.2023.121321.

[60] Mouffok A, Boublia A, Bellouche D, Zed SD, Tabhirt N, Alam M, et al. Investigating the synergistic effects of apple vinegar and deep eutectic solvent as natural antibiotics: an experimental and COSMO-RS analysis. Int J Environ Health Res 2024:1–22. https://doi.org/10.1080/09603123.2024.2370391.

[61] Boublia A, Guezzout Z, Haddaoui N, Badawi M, Lakikza I, Belkhettab I, Moumeni W, Aouni SI, Alam M, Benguerba Y. Comprehensive investigation of multifunctional polyaniline/reduced graphene oxide nanocomposites synthesized from deep eutectic solvents: Experimental, RSM, ANN and computational studies. Mater. Adv. 2024. https://doi.org/10.1039/D4MA00231H.

[62] Johnson ER, Keinan S, Mori-Sánchez P, Contreras-García J, Cohen AJ, Yang W. Revealing noncovalent interactions. J Am Chem Soc 2010;132:6498–506. https://doi.org/10.1021/ja100936w.

[63] Mandal S, Bej S, Banerjee P. Insights into the uses of two azine decorated d10-MOFs for corrosion inhibition application on mild steel surface in saline medium: experimental as well as theoretical investigation. J Mol Liq 2023;381:121789. https://doi.org/10.1016/j.molliq.2023.121789.

[64] Boutouil A, Laamari MR, Elazhary I, Bahsis L, Anane H, Stiriba SE. Towards a deeper understanding of the inhibition mechanism of a new 1,2,3-triazole derivative for mild steel corrosion in the hydrochloric acid solution using coupled experimental and theoretical methods. Mater Chem Phys 2020;241:122420. https://doi.org/10.1016/j.matchemphys.2019.122420.

[65] Yasmin T, Mahmood A, Farooq M, Sarfraz RM, Boublia A, Rehman U, et al. Development and evaluation of a pH-responsive Mimosa pudica seed mucilage/β-cyclodextrin-co-poly(methacrylate) hydrogel for controlled drug delivery: in vitro and in vivo assessment. Int J Biol Macromol 2024;268:131832. https://doi.org/10.1016/j.ijbiomac.2024.131832.

[66] Lu T, Chen F. Multiwfn: a multifunctional wavefunction analyzer. J Comput Chem 2012;33:580–92. https://doi.org/10.1002/jcc.22885.

[67] Humphrey W, Dalke A, Schulten K. VMD: visual molecular dynamics. J Mol Graph 1996;14:33–8. https://doi.org/10.1016/0263-7855(96)00018-5.

[68] Williams T, Kelley C. Gnuplot 4.5: an interactive plotting program, 56; 2011. URL, Http://Www.Gnuplot.Info.

[69] Arrousse N, Dioukhane K, Haldhar R, Salim R, hachmia E-E, Ichou H, et al. Electrochemical, theoretical, and surface adsorption studies of tetrazoles analogues of amino acids in acidic media. Mater Today Commun 2023;34: 105265. https://doi.org/10.1016/j.mtcomm.2022.105265.

[70] Fernine Y, Arrousse N, Haldhar R, Raorane CJ, Ech-Chihbi E, Kim SC, et al. Novel thiophene derivatives as eco-friendly corrosion inhibitors for mild steel in 1 M HCl solution: characterization, electrochemical and computational (DFT and MC simulations) methods. J Environ Chem Eng 2022;10:108891. https://doi.org/10.1016/j.jece.2022.108891.

[71] Fernine Y, Haldhar R, Arrousse N, Ebntouhami M, Taleb A, Kim SC, et al. Combined atomic-scale/DFT-theoretical simulations and corrosion protection study of AA2024-T3 in 3.5 % NaCl by phenolphthalein derivatives: surface characterization (FT-IR, FT-RAMAN, and SEM). J Electroanal Chem 2023;943: 117610. https://doi.org/10.1016/j.jelechem.2023.117610.

[72] Houssou A, Amirat S, Ferkous H, Alleg S, Dadda K, Boulechfar R, et al. Experimental and computational investigations on mechanically alloyed Fe55Co30Ni15 powders. Powder Technol 2024;433:119203. https://doi.org/10.1016/j.powtec.2023.119203.

[73] Zemouri AE, Bentouhami E, Zaghouane-Boudiaf H, Touahria YI, Bellil G, Boublia A, et al. Efficient wastewater decontamination using magnetic bentonite-alginate beads: a comprehensive study of adsorption dynamics, regeneration, and molecular interactions. J Environ Chem Eng 2024;12:113000. https://doi.org/10.1016/j.jece.2024.113000.

[74] Ferkous H, Zerroug M, Chaouch MA, Radjai M, Majdoub H, Bouzid A. Green corrosion inhibitor for carbon steel in 1 m hcl: a comparative study of polysaccharides extracted from prickly pear nopals of opuntia ficus-indica (peel and pulp). Adv Sci Technol Innov 2018;1293–6. https://doi.org/10.1007/978-3-319-70548-4_380.

[75] Sedik A, Athmani S, Saoudi A, Ferkous H, Ribouh N, Lerari D, et al. Experimental and theoretical insights into copper corrosion inhibition by protonated amino-acids. RSC Adv 2022;12:23718–35. https://doi.org/10.1039/d2ra03535a.

[76] Prifiharni S, Mashanafie G, Priyotomo G, Royani A, Ridhova A, Elya B, et al. Extract sarampa wood (Xylocarpus Moluccensis) as an eco-friendly corrosion inhibitor for mild steel in HCl 1M. J Indian Chem Soc 2022;99:100520. https://doi.org/10.1016/j.jics.2022.100520.

[77] Boulechfar C, Ferkous H, Delimi A, Berredjem M, Kahlouche A, Madaci A, et al. Corrosion inhibition of Schiff base and their metal complexes with [Mn (II), Co (II) and Zn (II)]: experimental and quantum chemical studies. J Mol Liq 2023; 378:121637. https://doi.org/10.1016/j.molliq.2023.121637.

[78] Arrousse N, Salim R, Benhiba F, Mabrouk EH, Abdelaoui A, El Hajjaji F, et al. Insight into the corrosion inhibition property of two new soluble and non-toxic xanthenbenzoate derivatives. J Mol Liq 2021;338:116610. https://doi.org/10.1016/j.molliq.2021.116610.

[79] Tawfik SM, Negm NA. Synthesis, characterization and evaluation of some anionic surfactants with phosphate group as a biodegradable corrosion inhibitor for carbon steel in acidic solution. J Mol Liq 2016;215:185–96. https://doi.org/10.1016/j.molliq.2015.12.030.

[80] Jebali Z, Ferkous H, Zerroug M, Boublia A, Delimi A, Bouzid A, et al. Unveiling the potent corrosion-inhibiting power of Ammophila arenaria aqueous extract for mild steel in acidic environments: an integrated experimental and computational study. J Environ Chem Eng 2024;12:112374. https://doi.org/10.1016/j.jece.2024.112374.

[81] Rouibah K, Ferkous H, Abdessalam-Hassan M, Mossab BL, Boublia A, Pierlot C, et al. Exploring the efficiency of Algerian kaolinite clay in the adsorption of Cr(III) from aqueous solutions: experimental and computational insights. Molecules 2024;29. https://doi.org/10.3390/molecules29092135.

[82] Lebouachera SEI, Balamane-Zizi O, Boublia A, Ghriga MA, Hasanzadeh M, El HH, et al. Understanding the factors affecting the adsorption of surface-active agents onto reservoir rock in chemical enhanced oil recovery applications: a comprehensive review. Chem Africa 2024. https://doi.org/10.1007/s42250-024-00931-4.

[83] Bousba D, Sobhi C, Zouaoui E, Rouibah K, Boublia A, Ferkous H, et al. Efficient biodiesel production from recycled cooking oil using a NaOH/CoFe2O4 magnetic nano-catalyst: synthesis, characterization, and process enhancement for sustainability. Energy Convers Manag 2024;300:118021. https://doi.org/10.1016/j.enconman.2023.118021.

[84] Kokalj A. Corrosion inhibitors: physisorbed or chemisorbed? Corros Sci 2022;196: 109939. https://doi.org/10.1016/j.corsci.2021.109939.

[85] Ituen E, Akaranta O, James A. Evaluation of performance of corrosion inhibitors using adsorption isotherm models: an overview. Chem Sci Int J 2017;18:1–34. https://doi.org/10.9734/csji/2017/28976.

[86] Roberge PR. Handbook of corrosion engineering. Choice Rev Online 2000;37:37. https://doi.org/10.5860/choice.37-5122. -5122-37–5122.

[87] Radjai M, Ferkous H, Zerroug M, Djellali S, Chaouch MA, Hattabi B, et al. Methanolic extract of artemisia herba alba as eco-friendly inhibitor of carbon steel corrosion in 1m hcl media. Adv Sci Technol Innov 2018;1379–81. https://doi.org/10.1007/978-3-319-70548-4_403.

[88] Lahbib H, Ben Hassen S, Gerengi H, Ben Amor Y. Inhibition effect of Cynara cardunculus leaf extract on corrosion of St37 steel immersed in seawater with and without bleach solution. Chem Eng Commun 2021;208:1260–78. https://doi.org/10.1080/00986445.2020.1771320.

[89] Madaci A, Ferkous H, Sedik A, Delimi A, Boulechfar C, Belakhdar A, et al. Experimental and theoretical study of polysaccharides extracted from prickly pear nopales Pulp (PPUN) of Opuntia ficus-indica as corrosion inhibitors. J Mol Liq 2023;384:122272. https://doi.org/10.1016/j.molliq.2023.122272.

[90] Ferkous H, Djellali S, Sahraoui R, Behloul H, Saoud K, Çukurovali A. 2-(2-Methoxybenzylidene) hydrazine-1-carbothioamide as efficient organic inhibitor for mild steel in hydrochloric acid solution. Environ Sci Eng 2021:1473–8. https://doi.org/10.1007/978-3-030-51210-1_235.

[91] Gao S, Brown B, Young D, Nesic S, Singer M. Formation mechanisms of iron oxide and iron sulfide at high temperature in H2S corrosion environment. NACE - Int Corros Conf Ser 2018:167–76. https://doi.org/10.1149/2.0921803jes. 2018-April.

[92] Djellali S, Ferkous H, Sahraoui R, Meharga S. Efficiency of alkaloids crude extract of cinnamomum zeylanicum as corrosion inhibitor of mild steel in sulfuric acid solution. Environ Sci Eng 2021:1379–84. https://doi.org/10.1007/978-3-030-51210-1_219. Springer.

[93] Zerroug M, Ferkous H, Radjai M, Chaouch MA, Madaci A, Majdoub H, et al. An afm study of the surface propriety and corrosion inhibition on carbon steel in acidic media. Adv Sci Technol Innov 2018:1337–9. https://doi.org/10.1007/978-3-319-70548-4_390. Springer.

[94] Dang YTH, Power A, Cozzolino D, Dinh KB, Ha BS, Kolobaric A, et al. Analytical characterisation of material corrosion by Biofilms J Bio- Tribo-Corros 2022;8:50. https://doi.org/10.1007/s40735-022-00648-2.

[95] Oguzie EE, Li Y, Wang F. Effect of surface nanocrystallization on the acid corrosion and corrosion inhibition of low carbon steel. Adv Mater Res 2008;38: 248–56. https://doi.org/10.4028/0-87849-390-5.248.

[96] Boublia A, Elboughdiri N, Georgin J, Yadav KK, Ghernaout D, Franco DSP, et al. Zinc chloride-assisted activation of açaí biomass for herbicide removal: insights from adsorption and molecular modeling. Process Saf Environ Prot 2024;188: 385–97. https://doi.org/10.1016/j.psep.2024.05.085.

[97] Neni A, Boublia A, Bouras M, Bentoumi A, Albrahim M, Elboughdiri N, et al. Evaluating asphaltene dispersion with choline chloride or menthol based deep eutectic solvents: a COSMO-RS analysis. J Mol Liq 2024;407:125272. https://doi.org/10.1016/j.molliq.2024.125272.

[98] Ait El Caid Z, Benmessaoud Left D, Kellal R, Safi ZS, Thoume A, Wazzan NA, et al. Green approach towards the corrosion suppression effect of carbon steel against an aggressive medium of 1 M HCl from peanut shells: electrochemical examinations coupled with theoretical insights. Mater Chem Phys 2024;316: 129081. https://doi.org/10.1016/j.matchemphys.2024.129081.

[99] El Caid ZA, Left DB, Zertoubi M. An exploratory assessment supported by experimental and modeling approaches for dinitrophenylhydrazine compound as a potent corrosion inhibitor for carbon steel in sulfuric acid solution. J Mol Struct 2024;1300:137218. https://doi.org/10.1016/j.molstruc.2023.137218.

[100] Ait El Caid Z, Benmessaoud Left D, Thoume A, Kellal R, Zertoubi M. Insight into the corrosion inhibition of dibenzylidene acetone for carbon steel in a sulfuric acid environment: synthesis, experimental, and theoretical studies. J Bio- Tribo-Corrosion 2024;10:9. https://doi.org/10.1007/s40735-023-00813-1.

[101] El CZA, DB L, Thoume A, Kellal R, Zertoubi M. A comprehensive computational study of N-phenylacetamide derivatives as corrosion inhibitors for copper: insights from DFT and molecular dynamics. J Bio- Tribo-Corros 2023;9:83. https://doi.org/10.1007/s40735-023-00803-3.

[102] Benzbiria N, Thoume A, Ait El Caid Z, Echihi S, Elmakssoudi A, Zarrouk A, et al. An investigation on the utilization of a synthesized benzodiazepine derivative as a corrosion inhibitor for carbon steel in sulfuric solution: chemical and electrochemical synthesis, surface analysis (SEM/AFM), DFT and MC simulation. Colloids Surf Physicochem Eng Asp 2024;681:132744. https://doi.org/10.1016/j.colsurfa.2023.132744.

[103] Z AEIC, D BL, Lgaz H, Seung LH, Zertoubi M. A multi-scale computational investigation of cationic dye interaction with rutile TiO2: an interconnected simulation approach. Inorg Chem Commun 2024;164:112425. https://doi.org/10.1016/j.inoche.2024.112425.

[104] Fuentealba P, Chamorro E, Santos JC. Chapter 5 Understanding and using the electron localization function. editor. Theor. Comput. Chem., vol. 19. Elsevier; 2007. p. 57–85. https://doi.org/10.1016/S1380-7323(07)80006-9.

[105] Tsirelson V, Stash A. Analyzing experimental electron density with the localized-orbital locator. Acta Crystallogr Sect B Struct Sci 2002;58:780–5. https://doi.org/10.1107/S0108768102012338.

[106] Gibbs GV, Cox DF, Boisen JB, Downs RT, Ross NL. The electron localization function: a tool for locating favorable proton docking sites in the silica polymorphs. Phys Chem Miner 2003;30:305–16. https://doi.org/10.1007/s00269-003-0318-2.

[107] Fuster F, Sevin A, Silvi B. Topological analysis of the electron localization function (ELF) applied to the electrophilic aromatic substitution. J Phys Chem A 2000;104:852–8. https://doi.org/10.1021/jp992783k.

[108] Fuentealba P, Chamorro E, Santos JC. Chapter 5 Understanding and using the electron localization function. Theor Comput Chem 2007;19:57–85. https://doi.org/10.1016/S1380-7323(07)80006-9.

[109] Kerkour R, Moumeni O, El houda Rabhi N, Mehri M, Boublia A, Chafai N, et al. Synthesis, DFT investigation, ADME-T properties, molecular docking and molecular dynamics simulation of new α-aminophosphonate inhibitor targeting Mpro and RdRp enzymes in SARS-CoV-2. J Mol Struct 2024;1315:138842. https://doi.org/10.1016/j.molstruc.2024.138842.

[110] Yasmin T, Mahmood A, Sarfraz RM, Rehman U, Boublia A, Alkahtani AM, et al. Mimosa/quince seed mucilage–co-poly (methacrylate) hydrogels for controlled delivery of capecitabine: simulation studies, characterization and toxicological evaluation. Int J Biol Macromol 2024;133468. https://doi.org/10.1016/j.ijbiomac.2024.133468.

[111] Zighed M, Benotmane B, Ferkous H, Ramdane N, Boublia A, Ahmed M, et al. Biodegradability assessment of HDPE-based biocomposites: influence of starch

and fiber composition. Mater Today Commun 2024:109786. https://doi.org/10.1016/j.mtcomm.2024.109786.

[112] Abdallah M, Al-Tass HM, Al Jahdaly BA, Fouda AS. Inhibition properties and adsorption behavior of 5-arylazothiazole derivatives on 1018 carbon steel in 0.5 M H2SO4 solution. J Mol Liq 2016;216:590–7. https://doi.org/10.1016/j.molliq.2016.01.077.

[113] Ferkous H, Rouibah K, Hammoudi NEH, Alam M, Djilani C, Delimi A, et al. The removal of a textile dye from an aqueous solution using a biocomposite adsorbent. Polymers (Basel) 2022;14:2396. https://doi.org/10.3390/polym14122396.

[114] Ferkous H, Delimi A, Kahlouche A, Boulechfar C, Djellali S, Belakhdar A, et al. Electrochemical and computational approaches of polymer coating on carbon steel X52 in different soil extracts. Polymers (Basel) 2022;14:1–20. https://doi.org/10.3390/polym14163288.

[115] Ferkous H, Delimi A, Kahlouche A, Boulechfar C, Djellali S, Belakhdar A, et al. Electrochemical and computational approaches of polymer coating on carbon steel X52 in different soil extracts. Polymers (Basel) 2022;14:3288. https://doi.org/10.3390/polym14163288.

[116] Rizi A, Sedik A, Acidi A, Rachedi KO, Ferkous H, Berredjem M, et al. Sustainable and green corrosion inhibition of mild steel: insights from electrochemical and computational approaches. ACS Omega 2023;8:47224–38. https://doi.org/10.1021/acsomega.3c06548.

[117] Dotto GL, Pinto LAA, Hachicha MA, Knani S. New physicochemical interpretations for the adsorption of food dyes on chitosan films using statistical physics treatment. Food Chem 2015;171:1–7. https://doi.org/10.1016/j.foodchem.2014.08.098.

[118] Pang X, Sellaoui L, Franco D, Netto MS, Georgin J, Luiz Dotto G, et al. Preparation and characterization of a novel mountain soursop seeds powder adsorbent and its application for the removal of crystal violet and methylene blue from aqueous solutions. Chem Eng J 2020;391:123617. https://doi.org/10.1016/j.cej.2019.123617.

[119] Dos Reis GS, Grigore Cazacliu B, Rodriguez Correa C, Ovsyannikova E, Kruse A, Hoffmann Sampaio C, et al. Adsorption and recovery of phosphate from aqueous solution by the construction and demolition wastes sludge and its potential use as phosphate-based fertiliser. J Environ Chem Eng 2020;8:103605. https://doi.org/10.1016/j.jece.2019.103605.

[120] Aouni SI, Ghodbane H, Merouani S, Lakikza I, Boublia A, Yadav KK, Djelloul C, Albakri GS, Elboughdiri N, Benguerba Y. Removal enhancement of persistent basic fuchsin dye from wastewater using an eco-friendly, cost-effective Fenton process with sodium percarbonate and waste iron catalyst. Environ. Sci. Pollut. Res. 2024. https://doi.org/10.1007/s11356-024-33845-2.

[121] Rouibah K, Ferkous H, Delimi A, Himeur T, Benamira M, Zighed M, et al. Biosorption of zinc (II) from synthetic wastewater by using Inula Viscosa leaves as a low-cost biosorbent: experimental and molecular modeling studies. J Environ Manage 2023;326:116742. https://doi.org/10.1016/j.jenvman.2022.116742.

[122] Goulart CM, Esteves-Souza A, Martinez-Huitle CA, Rodrigues CJF, Maciel MAM, Echevarria A. Experimental and theoretical evaluation of semicarbazones and thiosemicarbazones as organic corrosion inhibitors. Corros Sci 2013;67:281–91. https://doi.org/10.1016/j.corsci.2012.10.029.

[123] Xu B, Liu Y, Yin X, Yang W, Chen Y. Experimental and theoretical study of corrosion inhibition of 3-pyridinecarbozalde thiosemicarbazone for mild steel in hydrochloric acid. Corros Sci 2013;74:206–13. https://doi.org/10.1016/j.corsci.2013.04.044.

[124] Xu B, Yang W, Liu Y, Yin X, Gong W, Chen Y. Experimental and theoretical evaluation of two pyridinecarboxaldehyde thiosemicarbazone compounds as corrosion inhibitors for mild steel in hydrochloric acid solution. Corros Sci 2014;78:260–8. https://doi.org/10.1016/j.corsci.2013.10.007.

[125] Preethi Kumari P, Shetty P, Rao SA. Electrochemical measurements for the corrosion inhibition of mild steel in 1M hydrochloric acid by using an aromatic hydrazide derivative. Arab J Chem 2017;10:653–63. https://doi.org/10.1016/j.arabjc.2014.09.005.